Deficient Memory, Long-Term Potentiation and Hippocampal Synaptic Plasticity in Galectin-4-KO Mice.

María Elvira Brocca[1,*], Arancha Mora-Rubio[1], Elena Alonso-Calviño[2], Elena Fernández-López[2], Natalia Díez-Revuelta[1], Juan C. Guirado[1], Rebeca Álvarez-Vélez[4], Ana Dopazo[4], Esperanza López-Merino[3], David Martos-Puñal[1], José A. Esteban[3], Juan Aguilar[2,5] , Alonso M. Higuero[1,*] and José Abad-Rodríguez[1,*]

1-Membrane Biology and Axonal Repair Laboratory. Hospital Nacional de Parapléjicos (SESCAM), Instituto de Investigación Sanitaria de Castilla-La Mancha (IDISCAM). 45071 Toledo, Spain
2-Experimental Neurophysiology and Neuronal Circuits Laboratory. Hospital Nacional de Parapléjicos (SESCAM), Instituto de Investigación Sanitaria de Castilla-La Mancha (IDISCAM). 45071 Toledo, Spain
3- Laboratory of Synaptic Plasticity Mechanisms and Contribution to Cognitive Function. Department of Molecular Neuropathology, Centro de Biología Molecular Severo Ochoa (CSIC-UAM), 28049 Madrid, Spain.
4- Genomics Unit, Centro Nacional de Investigaciones Cardiovasculares (CNIC), Melchor Fernández Almagro, 3, 28029 Madrid, Spain.
5- Grupo de Investigación Multidisciplinar en Cuidados, Facultad de Fisioterapia y Enfermería, Universidad de Castilla-La Mancha, Toledo, Spain

* Correspondence may be addressed to *jabadr@sescam.jccm.es*, *ahiguero@sescam.jccm.es* and *mbrocca@sescam.jccm.es*

Keywords

Dendritic Spine, Galectin, Long Term Potentiation, Memory, Microbiota, Synapse.

Word count:

Abstract: 174
Main text: 8199
Figure legends: 1802

Abstract

Intestinal infections trigger inflammation and can contribute to degenerative and cognitive brain pathologies through the microbiota-gut-brain axis. Galectin-4 is an intestinal lectin key in the control of pathogenic bacterial infections. Here we report that galectin-4 deficient mice (Lgals4-KO) show an altered intestinal commensal microbiota in the absence of pathogens, defining a new role of galectin-4 in the modulation of commensal bacteria. Strikingly, Lgals4-KO mice present a deficient memory formation, and impaired hippocampal long-term potentiation (LTP) *in vivo* and *ex vivo*. Furthermore, Lgals4-KO neurons show a reduced activation of the AMPA receptor and of the CaMKII upon chemically induced LTP *in vitro*. These mice also display significantly lower dendritic spine density and shorter spine length in hippocampal dendrites, as well as an increased area of the postsynaptic densities, all coherent with an alteration of the synaptic function. In all, our results demonstrate that the absence of galectin-4 induces synaptic dysfunctions and memory impairment, along with changes in gut microbial composition, suggesting that variations in endogenous intestinal microbiota may cause or contribute to such neurological pathologies.

Brain function and many of its pathological conditions are influenced by biochemical or nerve signals that, originated in the gut, reach the central nervous system through the microbiota-gut-brain axis (Tran & Mohajeri, 2021; Benakis *et al*, 2020; Heijtz *et al*, 2011). Within the gut, epithelial glycans are a major component of the intestinal mucosa (Pelaseyed & Hansson, 2020; Johansson *et al*, 2013; Zhang *et al*, 2021) that regulate the interactions between the intestinal epithelium and the commensal or pathogenic bacteria. Similarly, bacterial surfaces are also heavily glycosylated, which allows glycans to serve as a crucial interface for integrating host, microbial, and environmental cues in the intestinal system (Kudelka *et al*, 2020). Alterations to glycans or glycan-based interactions can trigger the distortion of mucosal immunity and compromise the mucin barrier function, allowing deleterious interactions of infective microorganisms with host intestinal epithelium (Rausch *et al*, 2011; Fu *et al*, 2011; Tobisawa *et al*, 2010; An *et al*, 2007). Associated gut inflammatory or infectious processes have been linked to learning and memory dysfunctions, to mood disorders such as anxiety and depression, or to neurodegenerative pathologies such as Parkinson's and Alzheimer's diseases (Foster & Neufeld, 2013; Chu *et al*, 2019; Benakis *et al*, 2020).

Glycan-encoded information is translated into biological signalling by carbohydrate-binding proteins (lectins), among which, endogenous β-galactoside-binding lectins (galectins) play a central role in mammals (Barondes *et al*, 1994; Kasai & Hirabayashi, 1996). Galectin-4 (Gal-4) is a "tandem-repeat" type galectin holding two carbohydrate-binding domains (CRD) connected by a peptide linker (Rustiguel *et al*, 2016; Oda *et al*, 1993). This structure allows the cross-linking of glycosylated molecules containing β-galactoside moieties (Brewer, 2002), and other glycosylated or non-glycosylated epitopes such as O-linked sulfoglycans, sulfated glycosphingolipids, and cholesterol 3-sulfate (Ideo *et al*, 2005, 2002, 2007).

Gal-4 is prominently expressed by the epithelial cells of the intestinal tract, remaining intracellular or being secreted to the extracellular mucosa by non-classical secretory pathways as it is synthesized, like other galectins, without a signal peptide (Kutzner *et al*, 2020, 2022). In the intestinal environment, some pathogenic bacteria express on their surface glycosylated host-like antigens that cannot be detected by the adaptive immune system (molecular mimicry), thus they

can dock, proliferate, and invade the intestinal epithelium, triggering a cascade of intestinal malfunctions and secondary local immunological reactions (Jong *et al*, 2021). Gal-4, acting as a central effector of the innate immune system, targets and eliminates those pathogenic bacteria through its specific interaction with glycosylated self-antigens, either extracellularly at the gut mucosa as reported for *Escherichia coli* strains expressing human blood group antigens (Stowell *et al*, 2010, 2014; Acosta & Lepenies, 2019), or intracellularly in the intestinal epithelial cells infected with *Salmonella enterica,* where cytoplasmatic Gal-4 induces the formation of bacterial aggregates and restricts intracellular bacterial motility and spreading (Li *et al*, 2023). Despite its activity in the control of intestinal pathogenic bacteria, no role of Gal-4 in commensal bacteria regulation has been reported so far.

In the nervous system, some *in vitro* studies have described a very low expression of Gal-4 in immature neurons and oligodendrocytes and involved Gal-4 in myelination (Stancic *et al*, 2012; Wei *et al*, 2007; Díez-Revuelta *et al*, 2017), and axon growth (Velasco *et al*, 2013). However, we recently described that Gal-4 protein is undetectable in brain cortical tissue of wild-type mice, and that cortical myelin composition, structure and function are not altered in Gal-4-deficient mice (Lgals4-KO), disregarding both the nervous system expression and a possible role of Gal-4 on myelin regulation *in vivo* (Brocca *et al*, 2022).

We report here that Lgals4-KO mice show an altered intestinal commensal microbiota, unveiling a new function of Gal-4 as regulator of endogenous bacteria, in the absence of pathogens. This altered microbiota phenotype is concomitant with a deficient memory formation associated to an impaired long-term potentiation (LTP) in the hippocampus, a reduced postsynaptic signalling upon chemically induced LTP, and to significant alterations of the hippocampal dendritic spines and postsynaptic densities. Overall, these results point to an involvement of the intestinal commensal microbiota in regulating cognitive functions.

Results

Lgals4-KO mice present an altered intestinal microbiota composition with respect to WT animals

Given that Gal-4 is one of the most abundantly expressed anti-microbial lectins in the small and large intestine, we evaluated the effect of its absence on gut microbiota composition using a mouse knockout model. The analysis of the intestinal bacterial microbiota diversity between groups (beta diversity) showed significant differences between mouse strains according to all metrics applied (Bray-Curtis distance, Jaccard index, and unweighted UniFrac index) and determined by Permutational Multivariate Analysis of Variance (PERMANOVA, Adonis test; $p = 0.001$) (Fig. 1A, Fig. S1A and B).

The diversity within individual samples (alpha diversity) was evaluated using the Shannon index, Observed Features, Pielou's evenness, and Faith's Phylogenetic Diversity index. None of these metrics showed significant differences when analyzed using either a t-test or Wilcoxon rank-sum test (Fig. S1C).

After taxonomic assignment, the relative abundances at each taxonomic level were calculated (Fig. S2A and B). To identify differentially abundant taxa between groups, we performed an Analysis of Compositions of Microbiomes with Bias Correction (ANCOM-BC) and a Linear discriminant analysis (LDA) of Effect Size (LEfSe). From phylum to family level, relative abundances did not present significant variations according to ANCOM-BC. However, at the genus level, the Lgals4-KO microbiota present significant reductions of the genera *Peptococcus*, *UCG-009* and an unspecified genus of the *Prevotellaceae* family, while the *Paludicola* genus and the *Alistipes_timonensis* species were significantly increased (Figs. 1B and S2C).

In agreement, the LEfSe analysis revealed seven significantly increased and six significantly decreased bacterial species in Lgals4-KO mice (Fig.1C), including those identified by the ANCOM-BC analysis.

Overall, these results indicate that, although the within-sample diversity remains unchanged, the absence of Gal-4 expression results in a significantly altered gut microbial composition.

Memory formation deficits in Lgals4-KO mice

Changes in the gut microbiota composition can influence brain function as seen in microbiota depleted models (Vuong *et al*, 2016). Therefore, we conducted a series of behavioral tests to determine whether commensal microbiota variations

observed in Lgals4-KO mice could affect cognitive processes and depression and anxiety related behaviors.

To assess the hippocampus-dependent memory of Lgals4-KO mice we used the Y-maze Forced Alternation, Novel Object Recognition (NOR) and Object Location (OL) tests. First, WT and Lgals4-KO mice were tested using the Y-maze (Fig. 2A). Lgals4-KO mice spent significantly less time exploring the novel arm than WT mice (Mann-Whitney U test, WT median: 43.04, KO median: 26.55, ***p=0.0002) (Fig. 2B and 2C). Furthermore, it took Lgals4-KO mice a significantly longer time to enter the novel arm for the first time (Mann-Whitney U test, WT median: 11.08, KO median: 18.02, *p=0.0439) (Fig. 2D). Additionally, a greater proportion of Lgals4-KO mice did not prefer the novel arm as their first entry choice (82.0% and 64.9% correct choice for WT and KO, respectively), although this difference did not reach statistical significance (Chi-square test, p=0.0691) (Fig. 2E). These first results suggested that Lgals4-KO mice had an impairment in hippocampal-dependent memory formation. To corroborate these results, we subjected WT and Lgals4-KO mice to another memory task paradigm, the NOR test (Fig. 2F). In agreement with the Y-maze test results, Lgals4-KO mice spent less time exploring the novel object as reflected by a lower novelty preference score (61.5% and 46.3% for WT and KO, respectively) (Unpaired t-test, *p=0.0100) (Fig. 2G and 2H). Again, these results indicated that Lgals4-KO mice had an impaired memory formation. Lastly, we performed the OL test (Fig. S3A). In this case, both WT and Lgals4-KO mice explored similarly the familiar and novel locations as reflected by a similar novelty preference percentage (54.3% and 54.2% for WT and KO, respectively) (Mann-Whitney U test, WT median: 60.51, KO median: 56.24, p=0.8154) (Fig. S3A). This result suggests that both strains of mice had difficulties distinguishing between the novel and the familiar locations, preventing us from drawing any conclusions using this test.

Next, depression-like behavior was examined using the Porsolt forced swim test and the tail suspension test. In both tests, WT and Lgals4-KO mice spent similar percentages of time immobile, with no significant differences observed (Fig. S3B and C). Finally, we used the elevated zero maze test to assess anxiety-like behavior in Lgals4-KO mice. As before, there were no significant differences between strains in the percentage of time the mice spent in the open zones (Fig. S3D).

Taken together, our results show that mice lacking Gal-4 have an impaired recognition and spatial working memory, with no apparent alterations in anxiety- or depressive-like behaviors.

Impaired LTP induction in the hippocampus of Lgals4-KO mice

The induction of LTP in the hippocampus is a key indicator of proper memory formation and maintenance, thus memory deficiencies detected in Lgals4-KO mice could be associated with impaired LTP in the hippocampus.

To test if LTP induction was compromised in Lgals4KO-mice, we first performed extracellular recordings of excitatory postsynaptic field potentials (fEPSP) in acute brain slices of Lgals4-KO and WT mice. The fEPSPs were recorded in the *stratum radiatum* of the CA1 region of the hippocampus while Schaffer collaterals were stimulated to elicit synaptic NMDAR-dependent LTP responses in the presence of GABA receptors blockers (picrotoxin) (Fig. 3A).

The slope of the response in the basal transmission before stimulation did not report significant differences between mice strains (Fig. S4). However, the increase in the response upon LTP stimulation was significantly greater in control compared to knockout slices (Mann-Whitney U test, ***$p=0.0006$) (Fig. 3B, Post-LTP; 3C). These results pointed to a synaptic perturbation that prevents synapse strengthening upon stimulation, while basal synaptic function is apparently normal according to the unaltered basal transmission in Lgals4-KO hippocampus.

To further corroborate that LTP formation is defective in Lgals4-KO mice, the electrophysiological responses to LTP stimulation were measured *in vivo*. Stimulation electrodes were placed at the CA3 hippocampal region of anesthetized mice, while recording electrodes were located at the pyramidal layer of the contralateral CA1 hippocampal region (Fig. 3D). The stimulation pulses (30-50) were applied at the previously determined intensity to elicit LTP evoked response in CA1. Averaged responses were further processed and quantified. In good agreement with electrophysiological measures in acute brain slices (*ex vivo*), control brains (*in vivo*) produced a significantly higher response upon LTP stimulation than the normalized pre-stimulation values (Mann-Whitney U test, ****$p<0.0001$), while in knockout brains the LTP response upon stimulation was negligible and undistinguishable from basal level (Fig. 3E, Post-LTP; 3F). Put together,

electrophysiological results *ex vivo* and *in vivo* indicate that Lgals4-KO mice present alterations in the CA3-CA1 hippocampal pathway that significantly reduce the capacity of LTP generation.

WT and Lgals4-KO mice have comparable hippocampal neuronal densities and myelin expression and distribution

To gain insight into the underlying causes of the impaired memory phenotype and the deficient LTP induction in Lgals4-KO mice, we first determined whether the hippocampus of Lgals4-KO mice had equivalent morphological parameters as those of WT mice. Using anti-NeuN stained histological sections, we examined the volume of the hippocampus as well as the volume and neuronal densities of the CA1 and CA3 regions in both mice strains (Fig. S5A). Our results showed that hippocampal volumes and neuronal densities are comparable between WT and Lgals4-KO animals in all analyzed regions (Fig. S5B-D).

Oligodendroglia and activity-dependent myelin plasticity are also important modulators of many types and phases of learning and memory. They can influence information encoding, storage, and retrieval by modifying spike timing, axonal excitability, and the frequency and phase coupling of neural oscillations (Munyeshyaka & Fields, 2022). Oligodendrocyte function and myelin patterning are, in turn, altered by changes in the gut microbiota (Hoban *et al*, 2016; Lu *et al*, 2018; Needham *et al*, 2022). Given these considerations, we examined the state of hippocampal myelination in Lgals4-KO mice seeking for myelin perturbations that could account for the observed memory defects.

To do this, we first compared hippocampal myelin distribution using the Black Gold staining. No differences were found in the quantity or distribution of overall hippocampal myelin between WT and Lgals4-KO mice. This was also the case for segmented hippocampal zones (CA1, CA3, *hilus* and *stratum lacunosum moleculare*) (Fig. S6A). The number of Olig2-expressing oligodendrocytes in WT versus Lgals4-KO hippocampi also showed no differences in the whole hippocampus or segmented zones (Fig. S6B). Consistently, histochemical staining of major myelin markers, i.e. myelin basic protein (MBP; Fig. S6C, left column) and proteolipid protein 1 (PLP; Fig. S6C, right column) showed no variations in their expression or distribution between WT and Lgals4-KO mice. Supporting our histological results, the

hippocampal expression of selected relevant myelination markers such as MBP, MAG, CNP, MOG and Olig2 measured by western blot (Fig. S6D), or *Mbp*, *Plp*, *Mal*, *Sox10* and *Olig2* measured by RT-PCR (Fig. S6E) were similar in hippocampi from WT and Lgals4-KO mice. Furthermore, the expression of myelination-related genes assessed by hippocampal RNA-sequencing showed no significant differences between both mice strains (Fig. S6F).

In all, the exhaustive analysis of hippocampal myelination by different technical approaches indicates that the neurological phenotype evidenced by memory formation deficiencies in Lgals4-KO mice is not related to any perturbation of myelin composition, distribution, or architecture.

Reduced activation of GluA1 subunit and CaMKII upon chemical LTP stimulation of Lgals4-KO neurons

The phosphorylation of the GluA1 subunit of the NMDA receptor, and its delivery to the neuronal plasma membrane are main biochemical features of LTP induction (Shepherd & Huganir, 2007; Malinow, 2003). To test if GluA1 phosphorylation was affected by the lack of Gal-4, LTP was chemically induced (cLTP) in cultured mature hippocampal neurons, and GluA1 phosphorylation (S845) was analyzed in neuronal membrane extracts by western blot (Fig. 4A, Fig. S7A). The pGluA1/total GluA1 ratios upon cLTP induction were significantly lower in hippocampal neuron membranes of Lgals4-KO mice than in those of WT mice (Unpaired t-test, **p=0.0012) (Fig. 4A; light grey bars in graph). The incubation with recombinant Gal-4 before cLTP induction did not rescue this effect, suggesting an indirect implication of the lectin in synaptic function (Fig. 4A; dark grey bars in graph). In addition, AMPA receptor surface delivery upon cLTP induction was measured in cultured mature hippocampal neurons, by sequential immunocytochemical staining of the extracellular epitopes of GluA1 before permeabilization, and of the intracellular epitopes after permeabilization (Fig. 4B). In WT neurons, the surface GluA1/total GluA1 ratio significantly increased after cLTP induction (48,4%, Unpaired t-test, *p=0.0289), while no changes were evidenced in Lgals4-KO neurons (Fig. 4B, bar graph). These results are consistent with the reduced levels of phosphorylated GluA1 observed upon cLTP induction of Lgals4-KO neurons compared to WT neurons.

Activation of CaMKII in neurons is one of the first biochemical steps translating rapid Ca^{2+} raise into a long-lasting increase of synaptic strength during LTP and spine enlargement associated with LTP (structural LTP, or sLTP) (Lisman *et al*, 2012; Matsuzaki *et al*, 2004). To test if CaMKII activation is influenced by Gal-4 absence, its phosphorylation was quantified by western blot in membrane extracts of cultured mature hippocampal WT and Lgals4-KO neurons upon cLTP (Fig. 4C, Fig. S7B). While the normalized pCaMKII/CaMKII ratio augmented after LTP induction in WT neurons (Paired t-test, **p=0.0084), almost no effect was detected in Lgals4-KO neurons (Fig. 4C, light gray bars in graph). As it occurred in the case of GluA1 receptor subunit activation, the addition of recombinant Gal-4 to the cultures did not rescue the lack of activation of CaMKII in KO neurons (Fig. 4C, dark gray bars in graph). To further corroborate these results, brain slices of mice stimulated *in vivo* for LTP measurements (Fig. 3D-F) where submitted to immunofluorescence labelling of phosphorylated CaMKII. The level of pCaMKII, measured as pCaMKII positive area over a threshold in the CA1 hippocampal region (Fig. 4D, thresholded area), showed a significant raise upon LTP stimulation in WT mice, while it remained unaltered in Lgals4-KO mice (Two-way ANOVA, Sidak's multiple comparisons test: WT vs. WT+LTP, *p=0.0442; KO vs. KO+LTP, p=0.6959) (Fig. 4D, bar graph). In all, both biochemical and immunofluorescence results point to a deficient activation of CaMKII upon LTP stimulation in Lgals4-KO mice, which is consistent with the low activation of the GluA1 subunit of the NMDA receptor, and with the impaired LTP formation *ex vivo* and *in vivo*.

Reduced dendritic spine density and shorter dendritic spine length in apical and basal dendrites of Lgals4-KO neurons

LTP induction and consolidation have been related to the functional strengthening of existing synapses and/or the formation of new ones (Matsuzaki *et al*, 2004; Bosch & Hayashi, 2012; Gipson & Olive, 2017). We thus hypothesized that the deficient LTP induction in Lgals4-KO hippocampus could be caused by alterations at the synaptic level. Hippocampal expression of selected relevant pre-synaptic marker proteins such as synapsin 1 (SYN1), synaptotagmin 1 (SYT1), synaptophysin (SYP) and syntaxin 1A (STX1a), and the postsynaptic marker postsynaptic density 95 (PSD95), measured by western blot, were similar in WT and Lgals4-KO mice (Fig. S8A).

Moreover, RNA sequencing data confirmed that the expression of genes involved in synaptic processes showed no significant differences between both mice strains (Fig. S8B).

In the absence of differential expression of synaptic genes, synaptic alterations could be the result of structural variations. To approach this issue, the number and structural features of dendritic spines were compared in Golgi-Cox-stained brain slices of WT and Lgals4-KO mice (Fig. 5A and 5B). Spine density in basal and apical dendrites of CA1 hippocampal neurons was calculated by counting the number of spines in length-matched dendritic segments (10 **μ**m) (Fig. 5C). Both apical and basal dendrites of Lgals4-KO hippocampal neurons showed a significantly reduced spine density with respect to WT neurons (Apical: Unpaired t-test, ***$p < 0.0001$; Basal: Mann-Whitney U test, ***$p < 0.0001$) (Fig. 5C, bar graphs), regardless of the sex of the mice (Fig. S9). Immunohistochemical labelling of hippocampal tissue with Ionized calcium binding adaptor molecule 1 (Iba1), a pan marker for microglia/macrophages, revealed neither differences in microglia cell density, nor apparent morphological activation between WT and Lgals4-KO mice, indicating that low dendritic spine density in KO mice is not due to enhanced microglia-driven spine trimming (Fig. S10). To study eventual morphological effects on dendritic spines, the spine length and the width of the spine heads were manually traced and measured in each dendritic segment. The cumulative probability of both parameters was then calculated. These analyses indicated that dendritic spines from basal and apical dendrites of Lgals4-KO neurons were significantly shorter than those of WT neurons, as shown by the relative frequency distribution of spine lengths (Kolmogorov-Smirnov test, *$p<0.0001$) as well as by the comparison of the mean ranks of all measured spine lengths (Mann-Whitney U test, $p<0.0001$) (Fig. 5D). In contrast, no significant differences were detected in spine head widths (Fig. 5E).

Increased perforated synapses and enlarged postsynaptic density areas in Lgals4-KO neurons

A smaller hippocampal dendritic spine density could be associated to a lower number of synapses (Sorra & Harris, 1998)**,** which may account for the impaired memory formation and deficient LTP observed in Lgals4-KO mice. To determine whether this was the case, we quantified the hippocampal synaptic density using

transmission electron microscopy (TEM) images of hippocampal tissue (Fig. 6A). Our analyses showed no differences between WT and Lgals4-KO mice in total synapse density (Fig. 6A top) or "on shaft" synapses (Fig. 6A middle). In contrast, the density of high-efficiency perforated-type synapses is significantly increased in the hippocampus of Lgals4-KO mice (Unpaired t-test, **p=0.0011) (Fig. 6A bottom). Besides synapse density, the structural features of the postsynaptic densities are related to synaptic function (Borczyk *et al*, 2019; Sun *et al*, 2021; Harris, 2020). To assess structural postsynaptic differences, the cumulative frequency distributions of PSD areas and PSD lengths were calculated from measurements obtained from TEM images (Fig. 6B). This analysis showed a significant larger proportion of PSDs with an increased area in Lgals4-KO mice (Kolmogorov-Smirnov test; **p=0.0026), indicated by the rightward shift in the cumulative frequency plot (Fig. 6C, red line) and the comparison of all the measured PSD areas (Mann-Whitney U test; ***p<0.0001) (Fig. 6C, insert, red dots). In contrast, no differences were observed in the cumulative frequency distribution of PSD lengths (Kolmogorov-Smirnov test; p=0.1951) (Fig. 6D), or in the comparison of the mean ranks of PSD lengths (Mann-Whitney U test; p=0.1045) (Fig. 6D, insert).

Discussion

The intestine hosts the highest expression of galectin-4, making it one of the most abundantly expressed proteins in this organ, according to gene and protein expression databases (Fig. S11). Such a prominent presence in the intestine explains its central role in the control of pathogenic self-antigen-bearing bacteria within the intestinal lumen (Stowell *et al*, 2010; Li *et al*, 2023), although no role in the regulation of intestinal commensal bacteria had been reported so far. Using 16S rRNA sequencing, we detected significant differences in the composition of the bacterial populations between WT and Lgals4-KO mice (Fig. 1A, Fig. S1A, B), as well as in the relative abundance of several bacterial genera and species (Fig. 1B-C), demonstrating for the first time such a role of Gal-4 in this context.

A growing body of scientific literature links changes in the intestinal microbiota with the regulation of neurological functions and neuro-psychiatric pathologies through the microbiota-gut-brain axis (Foster & Neufeld, 2013; Chu *et al*, 2019; Benakis *et*

al, 2020). In the present study we submitted sex-balanced WT and Lgals4-KO mice cohorts to two blocks of behavioral tests, the first dedicated to evaluating the depression and anxiety-like behavior of mice (forced swim, tail suspension and elevated zero-maze), and the second focused on cognitive functions such as memory and learning (Y-maze, NOR and NOL). While no differences in the mood status (depression or anxiety) were observed in any of the applied tests (Fig. S3B-D), Lgals4-KO mice displayed a deficient performance in neurocognitive functions related to spatial memory formation and learning (Y-maze and NOR tests, Fig. 2) suggesting that Gal-4 could be connected to important cognitive processes related to hippocampal function. These core cognitive processes depend on the temporal patterns of neuronal circuits connecting diverse brain regions, which are regulated by myelination (Sugio *et al*, 2023; Bonetto *et al*, 2021). Even though myelin is unaltered in the cortex of Lgals4-KO mice (Brocca *et al*, 2022), local myelin alterations could still occur at the hippocampal level and account for cognitive failure. However, overall myelin expression, as well as myelin markers distribution in hippocampal tissue do not present significant differences between Lgals4-KO and WT animals (Fig. S6A-C). Moreover, most relevant myelin markers are similarly expressed at both protein and mRNA levels (Fig. S6D, E). In agreement, comparative transcriptomic analysis of hippocampal tissue revealed no significant differences in the expression of myelination-related genes (Fig. S6F). In all, unaltered hippocampal myelin in Lgals4-KO mice indicates that the observed memory deficiencies must be caused by myelin-independent mechanisms.

The most prominent physiological mechanism associated to memory formation and maintenance is the induction of LTP in the hippocampus (Nicoll, 2017). Thus, memory impairment in Lgals4-KO mice could involve defective LTP induction in this brain region. In fact, after stimulating the Schaffer collaterals in acute Lgals4-KO brain slices, the postsynaptic field potentials recorded in the hippocampal CA1 region were significantly lower than in WT slices (Fig. 3B and C). In consonance, high frequency stimulation of the CA3 region in living Lgals4-KO mice produced a weak response recorded in the contralateral CA1 area, again significantly smaller than in WT animals (Fig. 3E and F). As we hypothesized, these reduced responses to electrophysiological stimulation *ex vivo* and *in vivo* correspond to an impaired capacity to induce LTP in Lgals4-KO animals.

Even though LTP is a synapse-based process, we did not detect any differential expression of synaptic-related genes or proteins in Lgals4-KO mice (Fig. S8). In consequence, we explored expression-independent postsynaptic modifications such as the phosphorylation of AMPA receptors, one of the key post-translational events driving stable synaptic potentiation (Shepherd & Huganir, 2007; Malinow, 2003). More precisely, the stabilization of LTP depends on the retention of AMPA receptors in the membrane upon phosphorylation at position S845 of the intracellular region of the GluA1 subunit (Lee *et al*, 2010). Furthermore, the degree of stimulation following LTP induction is assumed to be proportional to the population of AMPA receptors in the postsynaptic membrane (Sumi & Harada, 2020; Chater & Goda, 2014). The significantly lower increase in GluA1-S845 phosphorylation after chemically-induced LTP in Lgals4-KO hippocampal neurons correlates with a reduced amount of the receptor on the neuronal membrane (Fig 4A, B). This would explain the inefficient synaptic potentiation observed in Lgals4-KO animals. Whether this is due to an impaired receptor trafficking towards the membrane or to a faster internalization of the AMPA receptors after stimulation remains unknown and would require further research.

AMPA receptor-facilitated Ca^{2+} influx into the postsynaptic neuron activates CaMKII through autophosphorylation (Lisman *et al*, 2012; Opazo *et al*, 2010), which in turn stimulates other signalling pathways (i.e. RAS-ERK) involved in memory formation (Park *et al*, 2016). Our results show lower CaMKII phosphorylation upon chemical induction of LTP in cultured Lgals4-KO hippocampal neurons. This is corroborated by lower pCaMKII signal in immunofluorescence staining of *in vivo* LTP-stimulated brain slices (Fig. 4C, D), all consistent with the observed neurological phenotype of memory deficit and impaired LTP.

The observation of these functional differences at the postsynaptic level raised the question of whether memory and LTP defects could be associated with morphological alterations in the postsynaptic structures. In fact, CA1 pyramidal neurons of Lgals4-KO mice display a sex-independent significant reduction in spine density in both basal and apical dendrites (Fig. 5A-C, Fig. S9), and these spines are significantly shorter compared to controls (Fig. 5D). It is important to note that microglial cell density, as well as the synaptic expression profile, is similar in the hippocampus of both mouse strains (Fig. S8 and S10). Therefore, neither spine

density nor spine length reductions are caused by increased microglial-driven spine trimming or an altered expression of synaptic proteins.

Despite a reduced dendritic spine density in KO mice, the synapse densities are similar in hippocampus of both mouse strains, as shown by synapse quantification in TEM images (Fig. 6A). Most likely, there is a higher proportion of spines forming synapses in the hippocampus of KO mice compared to WT mice. Additionally, in such a low dendritic spine density background, an increase in synaptic efficiency could also explain the normal basal neuronal activity shown by electrophysiological measurements (Fig. S4). Although we cannot determine whether the observed morphological differences are a primary consequence or an adaptive response, changes such as spine neck shortening (Noguchi *et al*, 2005) (Fig. 5D), an increased presence of high-efficiency perforated synapses (Fig. 6A, bottom) (Yamasaki *et al*, 2016), and larger postsynaptic density areas (Fig. 6B-C)(Borczyk *et al*, 2019; Sun *et al*, 2021; Harris, 2020) could contribute to overall higher synaptic efficiency. Importantly, these synaptic modifications in Lgals4-KO hippocampus, while maintaining basal synaptic activity, would limit further increases in synaptic efficiency in response to strong physiological demands, such as LTP stimulation, resulting in an impaired memory formation and cognitive deficits in Lgals4-KO mice.

The absence of Gal-4 protein expression in the brain of WT mice (Figs. S11 and S12), along with the absence of a rescue effect on cLTP induction by recombinant Gal-4 (Fig. 4A and C), indicates that the neurological alterations in Lgals4-KO mice are not directly caused by the loss of Gal-4 in the brain. Instead, these changes are likely signaled from outside the nervous system, primarily from the digestive tract, where Gal-4 is highly expressed and alterations in the composition of commensal microbiota are observed. The fact that all mice were fed the same diet and were housed in a controlled bacteriological environment minimizes the likelihood of pathogenic bacterial infections and likely explains the similar microbiota richness between the two mouse strains, as reflected by unchanged alpha-diversity indices (Fig. S1C). Nevertheless, there is a significant difference in the relative bacteria composition between mouse strains, indicated by beta-diversity analyses (Fig. 1A, S1A-B), with significant differences observed at the genus and species levels.

A reduced abundance of bacterial genus *Peptococcus* has been associated to diverse neurological conditions, including sleep disorders (Yan *et al*, 2024) and depression

(Palepu *et al*, 2024), both of which contribute to memory formation deficits (Chen *et al*, 2023; Yin *et al*, 2024). Consistently, Lgals4-KO mice exhibit a lower presence of *Peptococcus* (Fig. 1B) and deficient memory formation, reinforcing the association between this bacterial genus and impaired cognition.

Genera *Paludicola* and *Butyricicoccaceae_UCG009* are altered in mice fed with a high fat/high sugar diet (Pessoa *et al*, 2023), although no clear link to neurological disorders has been reported. Here, we provide evidence that Lgals4-KO mice on a standard diet, like control WT mice, show an increase in genus *Paludicola* and a reduction in genus *Butyricicoccaceae_UCG009* (Fig. 1B), concomitant with synaptic deficiencies and memory dysfunction.

Low levels of *Bacteroides acidifaciens* and *Bacteroides caecimuris* have been related to cognitive decline as well as to anxious and depressive behaviors in obese/insulin-resistant diabetic mice (Paiva *et al*, 2024; Mabrok *et al*, 2024) or after chronic stress (Zhang *et al*, 2024; Lin *et al*, 2024). Increased levels of these bacterial species in Lgals4-KO mice (Fig. 1C) may contribute to their normal performance in mood-related behavioral tests (Fig. S3B-D), although this increase would be insufficient to reverse memory deficits.

Furthermore, Lgals4-KO mice present a reduced presence of *Alistipes okayasuensis* (Fig. 1C), a recently described species related with poor outcomes in the DSS colitis mouse model (Forster *et al*, 2022). To our knowledge, this is the first report suggesting a connection between variations in *Alistipes okayasuensis* and neurological pathologies, including cognitive impairment.

How, and to which extent, these changes in intestinal microbiota/metabolite profile could signal through the pathways of communication between gut and brain (autonomic and enteric nervous systems, neuroendocrine and immune systems), remain unanswered questions. Addressing these questions will require deep metagenomic analyses of the microbiota and metabolomic studies. However, our findings strongly suggest that the altered profile of intestinal microbiota could underlie synaptic-associated memory and cognition failures in Lgals4-KO mice. Moreover, the fact that this occurs in the absence of pathogenic bacterial infections, defines a new role for Gal-4 in the regulation of commensal bacteria, and suggests that long-term imbalances in commensal bacteria, such as those caused by the lack

of Gal-4, could be sufficient to prompt significant neurological pathologies, a possibility with relevant clinical implications.

Material and Methods

Animals.

The Gal-4-deficient mice strain (C57BL/6NJ-Lgals4em1(IMPC)J/J), was purchased from The Jackson Laboratories. Homozygous animals are viable, fertile, and show a normal development and life span. C57BL/6NJ mice strain was used as WT control. Animals genotype was assessed by PCR *(Extended Experimental Procedures).* All experimental procedures involving animals were approved by the Animal Bioethics Committee (CEBA) of the Hospital Nacional de Parapléjicos-Research Center.

Intestinal microbiota analysis

Stool samples from 10 mice per strain (WT and Lgals4-KO), with equal numbers of males and females aged 6-7 months were collected, and total DNA was extracted using QIAamp Fast DNA Stool Mini Kit (Qiagen). The V3-V4 hypervariable region of the 16S rRNA gene was amplified through PCR, followed by the addition of sample-specific barcodes. Sequencing was performed on an Illumina MiSeq platform, generating 300 bp paired-end reads. The raw sequencing reads were processed using the DADA2 (v.1.32.0) pipeline in RStudio (v.2024.04.2+764, R v.4.4.0), including steps for quality filtering, trimming, dereplication, error correction, sequence variant inference, paired-end merging, and chimera removal. Taxonomic assignment was carried out using the SILVA database (version 138.1) with further species-level identification through exact comparisons with SILVA and NCBI reference datasets. A phylogenetic tree was constructed and the phyloseq package (v.1.48.0) in R was used for further analysis including the removal of non-microbial taxa. Alpha diversity was assessed using observed richness, Shannon diversity, Faith's Phylogenetic Diversity, and Pielou's Evenness. Beta diversity was analyzed via Principal Coordinate Analysis (PCoA) based on Bray-Curtis dissimilarity, Jaccard distance and Unweighted UniFrac distance metrics. The significance of beta diversity differences between groups was tested using adonis2 function (PERMANOVA) of the vegan package (v.2.6-6.1). Differential abundance of microbial

taxa between experimental groups was evaluated using Microbiome differential abundance and correlation analyses with bias correction (ANCOM-BC, v.2.6.0) and Linear discriminant analysis Effect Size (LEfSe) from the microbiomeMarker package (v.1.10.0), which identified taxa with significant differences and estimated their effect sizes.

Behavior tests

All sessions described were video recorded with automatic tracking of animal location and movements. *Y-Maze:* WT and Lgals4-KO mice were placed in the maze (three identical arms set at an angle of 120 degrees from each other) facing the end of the entry arm with the novel arm closed for a five-minute training session. 30 minutes after training the previously blocked novel arm was opened, and mice were allowed to explore all arms during the five-minute testing session. The number of arm entries, latencies and time spent in each arm were calculated during the period of maximal exploratory activity (first two-minutes) and submitted to statistical analyses. *Novel object recognition task (NOR) and object location task (OL):* The testing arena consisted of a square open field (50 x 50 x 50 cm), including visual cues in the walls. For habituation mice freely explored the arena for 15 min. The day after habituation, the NOR test was performed. Animals were submitted to two 10 minutes training sessions, during which they explored two objects with similar dimensions and shape but different materials, placed in adjacent corners of the arena. After a one-hour inter-trial interval for the NOR testing phase, one randomly selected object was replaced with a novel object in the original location. For the OL test, after similar training sessions and inter-trial interval than in the NOR test, one of the objects was moved to the opposite corner. In both cases, the time spent exploring each object over a 10 min testing period was calculated and data were analyzed. For this study, mice between 3 and 13 months were used (33 WT females, 21 KO females, 17 WT males and 16 KO males for Y maze test; 6 WT females, 7 KO females, 9 WT males and 8 KO males for NOR test; 6 WT females, 3 KO females, 8 WT males and 5 KO males for OL test). *Tail Suspension Test*: The tail suspension test was performed as previously described (Can *et al*, 2012) using a custom-made three-walled gray plastic apparatus (55 cm height x 60 cm width x 11.5 cm depth). Briefly, mice were suspended from a metal bar positioned at the top of the apparatus

using a tape strip securely adhered to their tail, and recorded during the 6 min test period. The total immobility time was calculated later for each animal by an observer blind to the genotype using the activity analysis feature of the Ethovision XT software. *Forced Swim Test*: The forced swim test was performed as previously described (Can *et al*, 2011). Mice were gently placed in glass cylinders (20 cm height x 16 cm diameter) filled with water at 24 ± 1 °C to a depth of 12 cm, and recorded during the 6 min test period, after which they were gently dried. The total immobility time was calculated later for each animal by an observer blind to the genotype using the activity analysis feature of the Ethovision XT software. *Elevated Zero Maze*: The test was performed using a circular (60 cm diameter) elevated zero maze apparatus (Ugo Basile). Mice were placed at the boundary between an open and closed zone, facing the inside of the closed zone, and recorded during the 5 min free-exploration test period. The time spent in the open zones of the maze was calculated for each animal by an observer blind to the genotype using the tracking feature of the Ethovision XT software. Further details on behavior tests in *Supplementary Information*.

RT-PCR and RNA-seq

Hippocampi from 30-day-old mice were stored in RNAlater (Invitrogen) at -20°C until processing. Total RNAs were extracted using RNeasy Mini Kit (Qiagen) adding DNAse (Pure Link DNAse, Invitrogen) during column washing. Extracted RNA was quantified spectrophotometrycally (Nanodrop Technology) and RNA quality was assessed in a Bioanalyzer 2100 (Agilent Technologies).

RT-PCR: cDNA was synthesized with High-Capacity RNA to cDNA kit (Applied Biosystems). Expression was measured by RT-PCR (7900HT system, Applied Biosystems) using appropriate TaqMan probes (Applied Biosystems, Supplementary Table S2). Each sample was analyzed in duplicate. Housekeeping genes (GAPDH and β-actin) were used to normalize mRNA expression levels. The relative amounts of mRNA were calculated using the $2^{(-\Delta\Delta CT)}$ method (Livak & Schmittgen, 2001)

RNA-seq: 100 ng of total RNA were used to generate barcoded RNA-seq libraries using the NEBNext Ultra II Directional RNA Library preparation kit (New England Biolabs) according to manufacturer's instructions. First, poly A+ RNA was purified

using poly-T oligo-attached magnetic beads followed by fragmentation and first and second cDNA strand synthesis. Next, cDNA ends were repaired and adenylated. The NEBNext adaptor was then ligated followed by second strand removal, uracil excision from the adaptor and PCR amplification. The size of the libraries was checked using the Agilent 2100 Bioanalyzer and the concentration was determined using the Qubit® fluorometer (Life Technologies). Libraries were sequenced at 2.5 nM on a HiSeq 4000 (Illumina) to generate 61 bases single reads. FastQ files for each sample were obtained using bcl2fastq 2.20 Software (Illumina).

Neuron cultures and cLTP induction.

Primary mouse hippocampal neuron cultures were obtained from P17 embryos as previously reported (Goslin *et al*, 1998). Briefly, the hippocampi were dissected, mechanically disrupted and trypsinized. Pelleted cells were resuspended in MEM-HS-0.6% glucose and seeded onto poly-L-lysine (PLL)-coated plastic Petri dishes, or onto PLL-coated glass coverslips. Cells were allowed to adhere, and the medium was then changed to Neurobasal supplemented with 2% B-27 and glutamine. Cultures were maintained at 37°C and 5% CO2. Cells were incubated or not for 2 hours with 0.75 mg/mL recombinant human Gal-4, before chemical induction of LTP. For chemical induction of LTP, neurons were pre-incubated in artificial cerebrospinal fluid (ACSF, 15 min, 37 0C, 5% CO2), and LTP was stimulated in Mg2+-free ACSF supplemented with 0.1 μM rolipram, 50 μM forskolin and 100 μM picrotoxin (15 min, 37 0C, 5% CO2). Neurons on coverslips were further processed for immunocytochemistry, and neuron extracts for biochemical analyses were obtained from cultures on Petri dishes. *Immunocytochemistry and quantification of surface GluA1:* Neurons in culture were fixed with 4% PFA and 4% sucrose in PBS at RT. Non-specific binding was blocked with 0.2% gelatine and 1% BSA in PBS. For the labelling of surface GluA1, neurons were incubated for 2 h with an antibody against the GluA1 N-terminal extracellular domain. After membrane permeabilization step with 0.1% Triton X-100, 0.2% gelatine and 1% BSA in PBS, total GluA1 was labelled by 1 hour at RT incubation with an antibody against the GluR1 intracellular C-terminal domain. After thorough washing with PBS, cells were incubated for 1 hour with the appropriate anti-species antibodies conjugated to Alexa Fluor 555 or Alexa Fluor 647 (Life Technologies). Coverslips were mounted onto glass slides using

Permount (Life Technologies). Cells were imaged using a confocal microscope (LSM800; Carl Zeiss) and quantification was performed using ImageJ software. Regions of interest (ROIs) corresponding to individual dendrites were selected on the total GluA1 channel. Thus, image quantification was blind with respect to the surface GluA1 channel. Image channels were split and thresholded separately. Channel background was measured in 3 free-of-signal ROIs/image, averaged, and subtracted from total channel fluorescence signal. Fluorescence intensity was then measured in every ROI and surface GluA1/total GluA1 ratios were calculated. 10 images per condition, and between 5 and 10 ROIs/image were quantified in each of 3 independent experiments.

Electrophysiology

Brain slices (ex vivo): Mice were anesthetized and quickly decapitated. Dissected brains were submerged in Ca^{2+}-free ice-cold dissection solution saturated with carbogen (5% CO_2, 95% O_2). Vibratome coronal slices (350 µm) were submerged in carbogen-gassed aCSF and transferred to an immersion chamber placed on the microscope plate under continuous carbogen-gassed aCSF perfusion. Field excitatory postsynaptic potentials (fEPSPs) were recorded from CA1 *stratum radiatum* while stimulating Schaffer collateral fibers (50 µs pulses, 20-250 µA). For all experiments aCSF was supplemented with 100 µM picrotoxin to block GABAA receptors. Data acquisition was carried out with MultiClamp 700A/B amplifiers and pClamp software (Molecular Devices). For time course representations, responses were grouped in 60 second bins and normalized to the average baseline response.

Living animal (in vivo): Animals were anesthetized with isofluorane and submitted to craniotomies over stereotaxic coordinates of hippocampal regions of pyramidal layer in CA1 (recording electrode), and contralateral CA3 (stimulation electrode). Square electrical 50 µs stimulation pulses, using increasing steps of intensities (0.1 to 1mA), were applied to detect the threshold of response in contralateral CA1, which was considered the stimulation intensity at which the populational response was evoked by 50% of stimuli. This threshold intensity was used to obtain the local field potentials (LFPs) during the entire protocol. Electrophysiological recordings were digitalized and analyzed to quantify the response magnitudes of the populational spike recorded in the pyramidal layer of CA1 in response to CA3

stimulation (LFP unfiltered signal) across the entire stimulation protocol. All response magnitudes obtained for each single stimulus from each animal were normalized to the population responses average. Statistical comparisons (Paired t-test) were carried out for intra-group effects between baseline and post-LTP condition, and for inter-groups in the same condition. Methods and data analysis procedures on electrophysiological studies are detailed in *Supplementary Information*.

Histochemistry and Immunohistochemistry

Tissue sampling: Mice were anesthetized with sodium pentobarbital, perfused, and brains and intestines were collected. For immunohistochemistry (IHC) and black gold staining, tissues were post-fixed (16 hours, 4°C), incubated in PBS for 24 h, cryoprotected in Olmos solution (30% ethylene glycol, 0.6 M sucrose and 10 g PVP-40 in 0.1 M phosphate buffer) and stored at -20°C. Brain serial coronal sections (40 µm thick) were collected using a vibrating blade microtome (Leica VT1200/VT1200S). For immunofluorescence (IF), mouse tissues were post-fixed in 4% PFA overnight at room temperature and then embedded in paraffin. Sections (2 µm-thick) were deparaffinized prior to immunolabelling. In the case of pCamkII IF, brains from mice subjected or not to electrophysiological LTP induction were perfused after electrophysiological recordings. Brains were post-fixed, cryoprotected, frozen and cryosectioned (20 µm thick). For the study of dendritic spines, entire brains of 5 female and 5 male (7 months old) mice from both strains were dissected and submitted to Golgi-Cox staining.

Immunostainings: For fluorescent staining, sections were blocked (1h, RT) and incubated (16 hours, 4°C) with the indicated primary antibodies (Supplementary Table S1 for antibodies). Upon thoroughly washing, sections were incubated (90 min, RT) with fluorophore-conjugated anti-species antibody. Nuclei were counterstained with DAPI, and slices were coverslipped. For immunochemical staining endogenous peroxidase activity was previously inactivated blocked. Sections were then incubated (16h, 4°C) with primary antibodies in blocking solution, thoroughly washed, and further incubated (2 hours, RT) with the appropriate biotinylated anti-species antibody. Staining was visualized with Vectastain Elite ABC Kit Peroxidase (Vector), and sections were dehydrated in

ethanol gradient, clarified in xylene and mounted with DPX mounting medium (Sigma-Aldrich).

Black Gold staining: The Black Gold II Myelin staining kit (#AG105, Millipore) was used according to manufacturer's instructions. Concisely, brain serial sections were dried, rehydrated and incubated in 0.3% Black-Gold II solution (60°C, 40 min). After rinsing in water, slides were incubated (3 min, 60°C) in 1% sodium thiosulfate and further washed, dehydrated, cleared, and mounted as before.

Golgi-Cox staining: The FD Rapid GolgiStain™ Kit (FD NeuroTechnologies) was used following the manufacturer's instructions with minor modifications. Briefly, unfixed brains were immersed in the impregnation solution (A/B, 2 weeks), and incubated in solution C (2 days). Brains were then frozen in isopentane at -80ºC, cryosectioned (100 µm thick) and mounted on gelatin-coated microscope slides. Sections were incubated in D/E solutions, washed, dehydrated, cleared and mounted as before.

Image segmentation and analysis: For Olig2 and Gal-4 IF, images were acquired with 10X and 40X objectives, respectively. For GFAP and Iba1 IHC staining, images were acquired with a 40X objective. An Olympus IX83 microscope was used in all cases. For MBP and PLP IHC, and for black gold staining, bright field images were taken with the 20x objective of an Olympus BX61 microscope, using the newCAST software. For all IHC analyses, ROIs encompassing hippocampus CA1, CA3, *stratum lacunosum moleculare* (Lm) and *hilus* were traced using ImageJ software and based on the Mouse Brain Atlas as reference. For pCamkII immunodensity measurement, Z-stacks (step size: 0.5 µm) were acquired on a confocal microscope (Leica SP5, Leica Microsystems, Germany). Image analyses and processing were performed using the ImageJ software by researchers blinded to experimental conditions. For the study of spine density and spine morphology, Z-stack images (0.56 µm optical section thickness) of Golgi-Cox stained CA1 hippocampal neurons were acquired using an Olympus IX83 P2ZF microscope with a 60x / 1.42 objective. Only completely stained isolated neurons with at least third-order dendritic branches were selected for this study. 2984 apical and 2575 basal spines were morphologically analyzed, distributed in four sex/strain groups. Other exclusion criteria, statistical analyses and group composition are detailed in *Extended Experimental Procedures* and in (Brocca *et al*, 2013).

Transmission electron microscopy

Lgals4-KO and control animals (8 months old) were anesthetized with sodium pentobarbital and transcardially perfused with saline followed by 4% PFA + 2% glutaraldehyde in 0.1 M phosphate buffer (PB) at pH 7.4. Brains were post-fixed at RT for 2h and ON at 4 °C, thoroughly washed in PB buffer, and coronal sections encompassing the dorsal CA1 region of the hippocampus (Bregma -1.34mm to -2.06mm) were obtained at 200 um thickness using a vibrating microtome (Leica VT1200). Vibratome sections were postfixed with 1% osmium tetroxide and 0.8% aqueous potassium ferricyanide solution for 1h at 4 °C. After rinsing, samples were incubated with 0.15% tannic acid for 1 min at RT, 2% uranyl acetate for 1h at RT, dehydrated in a graded series of ethanol solutions at 4 °C, and embedded in epoxy resin (TAAB 812, TAAB Laboratories). Serial ultrathin sections (70 nm) were cut with an ultramicrotome Ultracut E (Leica), mounted on Formvar-carbon-coated Cu/Pd slot grids, and stained with 2% uranyl acetate and lead citrate. Samples were examined on a JEM-1400 Flash transmission electron microscope (Jeol, Japan) at 100 kV, with a Oneview 4K x4K CMOS camera (Gatan, Pleasanton, CA USA).

Synaptic density was quantified in the stratum radiatum of hippocampal CA1 using the unbiased physical dissector method (Sterio, 1984). Each dissector consisted of photomicrographs from the same position in two consecutive ultrathin sections, a reference and a look-up section. Synapses were identified by the presence of a postsynaptic density and a presynaptic terminal containing synaptic vesicles, separated by a synaptic cleft. Perforated synapses were defined by the presence of a discontinuity in the postsynaptic density. Only synapses present in the reference section but absent in the look-up section, or vice versa, were manually counted by an observer blind to the genotype of the animal using ImageJ software. Synaptic density was calculated by dividing the number of synapses counted per dissector by the volume of the dissector (given by the frame area × dissector thickness). The dissector height was 140 nm. The total volume examined was 869.6 and 927.9 μm^3 for WT and Lgals4-KO groups, respectively; and the total number of synapses counted was 2143 and 2540 for WT and Lgals4-KO groups, respectively.

The lengths and areas of PSDs were quantified using a combination of manual annotation, deep learning, and image analysis software. A total of 90 micrographs were manually annotated using the "Training Labels" tool in OlyVia software

(Olympus), where the PSD membrane, PSD area, and background regions were labelled. These annotated micrographs served as the training set for a convolutional neural network (CNN) based on the U-Net architecture, utilizing Olympus' TruAI extension within the cellSens software (Olympus). The neural network training was configured with Balanced data sampling, Local Contrast normalization, Softmax cross-entropy loss, and the Adam optimizer. Data augmentation involved 90-degree rotations and mirroring to enhance model generalization, with no additional image processing augmentation applied. Training was conducted for 250,000 iterations with a similarity threshold of 0.71, using 10 of the 90 images for validation, with a scaling factor of 25, and checkpoints saved every 6 epochs. Post-training, the trained model was applied to the remaining micrographs for automated detection and segmentation of PSDs. To ensure accuracy and precision, every segmented image was reviewed by trained researchers blinded to the genotype of the animals and, when necessary, manually corrected in ImageJ to ensure that the segmented lengths and boundaries accurately captured the dimensions of the PSDs. Final measurements of PSD lengths and areas were obtained using a custom macro in ImageJ.

Data, Materials, and Software Availability. All study data are included in the article and/or *Supplementary information,* or available upon justified request to corresponding authors.

Acknowledgments

We want to thank the staff of the microscopy, proteomics, and animal house facilities at the Hospital Nacional de Parapléjicos –SESCAM- (Toledo, Spain) for their valuable technical support, and to Dr. Rafael Luján for his helpful advice on TEM images interpretation. This work was supported by (1) grant PID2021-125428OB-I00; funded by MCIN/AEI/10.13039/501100011033 and by "ERDF A way of making Europe"; (2) grant SAF2017-83821-R; funded by MCIN/AEI/10.13039/501100011033 and by "ERDF A way of making Europe"; (3) grant PID2019-105020GB-100; funded by MCIN/AEI/10.13039/501100011033 and by "ERDF A way of making Europe"; (4) grant SBPLY/17/180501/000250; funded by Consejería de Educación, Cultura y Deportes de Castilla La Mancha (Spain); (5) AMR holded a predoctoral fellowship grant SBPLY/19/180501/000407, funded by "Consejería de Educación, Cultura y

Deportes de Castilla La Mancha", and co-funded by the European Social Fund (Fondo Social Europeo "El FSE invierte en tu futuro").

Figure legends

Fig. 1. Lgals4-KO mice have an altered microbiota composition. (A) Principal coordinate analysis (PCoA) plot of bacterial beta diversity based on the Bray-Curtis distance. Gut microbiota samples from WT and Lgals4-KO mice show a significantly different sample distribution between groups (Adonis, p=0.001). The black dots represent WT while the grey dots represent Lgals4-KO samples. Ellipses indicate 95% confidence interval, and the percentages in parentheses are the proportion of variation explained by the PCoA axis. Animals used: WT n=10, KO n=10. (B) Lollipop plot showing the differentially abundant taxa identified by ANCOM-BC analysis. Each line indicates a differentially abundant taxon, with the line length reflecting the magnitude of the log fold change and a circle at the end marking the exact value. Lgals4-KO enriched and depleted taxa are represented as blue and red lines, respectively. (C) Differentially abundant taxa identified by LEfSe analysis. Histogram representation of the LDA scores for the differentially abundant taxa between WT and Lgals4-KO groups. The length of the bar represents the log10 transformed LDA score. WT and Lgals4-KO enriched taxa are represented in white and grey bars, respectively.

Fig. 2. Lgals4-KO mice display an impaired hippocampus-dependent spatial memory formation. (A) Schematic representation of the Y-maze test. (B) Representative heatmaps of the cumulative time mice spent exploring each of the three arms of the Y-maze for WT (left) and KO (right) mice during the testing session. Warm and cold colors are indicative of more and less time spent exploring each arm, respectively. (C) Bar graph representing the percentage of total time that mice spent exploring the novel arm. Lgals4-KO mice spent significantly less time exploring the novel arm (Mann-Whitney U test; ***p=0.0002). The dashed line at 33% represents the percentage of time mice would randomly explore any of the three arms. (D) Bar graph showing that Lgals4-KO mice display a higher latency to explore the novel arm (Mann-Whitney U test; *p=0.0439). (E) Stacked bar graph

representing the percentage of correct and incorrect first arm entry choices. There is no difference in the proportion of correct first arm entry choices between WT and Lgals4-KO mice (Chi-square test; p=0.0691). (F) Schematic representation of the NOR test. (G) Representative heatmaps of the cumulative time mice spent exploring the novel and familiar objects for WT (left) and KO (right) mice. Warm and cold colors are indicative of more and less time spent exploring each object, respectively. (H) Bar graph showing that Lgals4-KO mice spent significantly less time exploring the novel object expressed as a percentage of Novelty Preference (Unpaired t-test; *p=0.0100). The dashed line at 50% represents the percentage of time mice would randomly explore any of the two objects. All represented data are means + SEM. Animals used for the Y-maze test: WT n=50, KO n=37; for NOR test: WT n=15, KO n=15.

Fig. 3. Impaired long-term potentiation of synaptic strength in Lgals4-KO mice. (A) Schematic representation of the induction and recording of LTP in acute hippocampal slices. Responses were evoked by stimulating Schaffer collaterals and recorded from CA1 *stratum radiatum*. (B) Time course of LTP induced by theta-burst stimulation (TBS, black arrow) in WT and Lgals4-KO hippocampal slices. (C) Bar graph shows a statistically significant reduction in the average change in fEPSP slope from the last 25 min of the recording in Lgals4-KO slices compared to control (Mann-Whitney U-test, ***p=0.0006). Dots represent the number of recordings (WT n=14 from 14 slices; KO n=19 from 17 slices) obtained from 9 mice per condition. (D) Diagram of a mouse hippocampus with electrodes in place for the induction and recording of LTP in anesthetized animals *in vivo*. Stimulation was performed in CA3 and responses were recorded in the contralateral CA1 region. (E) Time course of LTP induced by high-frequency stimulation (HFS, black arrow) in WT and Lgals4-KO mice. Pre and post-LTP responses were recorded with a 60 min gap after stimulation. (F) Bar graphs show a statistically significant increment in the amplitude of post-LTP responses in WT mice but not in Lgals4-KO mice (Wilcoxon signed rank test, WT ****p<0.0001; Paired t-test, KO p=0.2271). Dots represent the mean normalized amplitude values for each of the 16 stimuli before and after LTP induction obtained from 12 WT and 21 Lgals4-KO mice. Data are means ± SEM.

Fig. 4. Reduced activation of GluA1 receptors and αCaMKII after LTP induction in Lgals4-KO mice. (A) Representative western blot of GluA1 S845 phosphorylation (pGluA1) before (-) and after (+) cLTP induction in WT and Lgals4-KO hippocampal neuron lysates. To assess a potential rescue effect, cell lysates were incubated with recombinant Gal-4 (Gal-4 +).Total GluA1 and β-actin are shown as loading controls used for normalization. Bar graph shows the quantification of the ratio of pGluA1/GluA1 levels in WT and Lgals4-KO lysates before and after cLTP induction with or without the addition of recombinant Gal-4. Lgals4-KO neuron lysates display reduced pGluA1/GluA1 levels after cLTP induction compared to WT neurons (Paired t-test; **p=0.0012) which is not reversed by the addition of recombinant Gal-4 (Paired t-test; **p=0.0012). Bars represent the mean ratio + S.E.M. normalized to the basal conditions (Gal-4 -; cLTP -). Results were obtained from at least 3 different cultures. (B) Representative images of DIV14 cultured neurons before and after cLTP induction immunostained for surface GluA1 receptors (green) without a permeabilization step. Cells were then fixed, permeabilized and immunostained for total GluaA1 using an antibody that recognizes an intracellular epitope (red). Dashed white rectangles depicting total and surface GluA1 are magnified and shown as grayscale images at the right of their corresponding condition. Scale bars: 25 μm (whole images), 5 μm (magnifications). Bar graph shows a significant increase in the ratio of surface/total GluA1 receptor levels in WT (Unpaired t-test; *p=0.0289) but not in Lgals4-KO (Unpaired t-test; p=0.3212) cultures after cLTP induction. Bars represent the mean ratio + S.E.M. obtained from at least 3 different cultures. (C) Representative western blot of T286 phosphorylated αCaMKII (pCaMKII) before (-) and after (+) cLTP induction in WT and Lgals4-KO hippocampal neuron lysates. Cell lysates were incubated with recombinant Gal-4 (Gal-4 +) to evaluate a possible rescue effect. Total αCaMKII and GAPDH are shown as loading controls used for normalization. Bar graph shows the quantification of the pCaMKII/total αCaMKII levels ratio in WT and Lgals4-KO lysates before and after cLTP induction with and without the addition of recombinant Gal-4. Lgals4-KO neuron lysates display reduced phosphorylated/total αCaMKII levels after cLTP induction compared to WT neurons (Paired t-test; **p=0.0084) which is not reversed by the addition of recombinant Gal-4. Bars represent the mean ratio + S.E.M. normalized to the basal conditions (Gal-4 -; cLTP -). Results were obtained from at least 3 different cultures.

(D) Representative immunofluorescence images of T286-autophosphorylated αCaMKII (green) in the dorsal CA1 region of control and LTP-induced WT and Lgals4-KO mice (upper panels). The immunopositive area was segmented in the whole image after applying a signal threshold (lower panels). Scale bars: 25 μm. Bar graph shows the quantification of pCaMKII immunopositive area for control WT and Lgals4-KO mice and those subjected to LTP induction *in vivo*. LTP induction leads to a T286-autophosphorylation increase in WT but not in Lgals4-KO mice (Two-way ANOVA; effect of strain, $F(1,25) = 4.291$, $p=0.0488$; effect of LTP induction, $F(1,25) = 5.465$, $p=0.0277$; Sidak's multiple comparisons test: WT vs. WT+LTP, *$p=0.0442$; KO vs. KO+LTP, $p=0.6959$). Dots represent the mean value of all sections analyzed per animal (WT n=6, WT+LTP n=6, KO n=6, KO+LTP n=11). Data are mean + SEM.

Fig. 5. Reduced dendritic spine density and altered morphology in Lgals4-KO mice. (A) Representative mosaic image of a Golgi-Cox-stained mouse brain hemisphere. The Golgi-Cox staining technique enabled the visualization of the distribution of isolated pyramidal neurons in the hippocampal CA1 region. Scale bar: 500 μm. (B) Representative microphotograph of a fully stained CA1 pyramidal neuron showcasing its abundant arborization. The basal branches extend towards the stratum oriens and the apical branches reach the stratum radiatum. Scale bar: 50 μm. (C) Illustrative images highlighting Golgi-Cox stained apical (left panels) and basal (right panels) dendrites at high magnification. The images display numerous basal and apical spines in WT mice, while a reduced number of both apical and basal spines is evident in Lgals4-KO mice. Scale bar: 10 μm. The bottom bar graphs show the dendritic spine density within the CA1 subfield. The apical and basal dendritic spines exhibited a significantly lower density in Lgals4-KO compared to WT mice (Apical: Unpaired t-test, ***$p< 0.0001$; Basal: Mann-Whitney U test, ***$p< 0.0001$). All measured data are expressed as means + SEM of 10 animals per strain. (D) Cumulative frequency distribution of spine lengths of both apical and basal dendrites. Note that the cumulative frequency plot for spine lengths is always shifted leftward in Lgals4-KO mice, indicating a greater proportion of shorter spines (Kolmogorov-Smirnov test; *$p<0.0001$). The inset represents a scatter plot of each spine length value included in the analysis for both strains (Mann-Whitney U test; $p<0.0001$). (E) Cumulative frequency distribution of spine head widths from apical

and basal dendrites. Golgi-stained spines exhibited comparable head widths across both experimental groups in both apical and basal dendrites (Kolmogorov-Smirnov test). The inset displays a scatter plot of the individual head width values measured for both WT and Lgals4-KO mice (Mann-Whitney U test).

Fig. 6. Increased number of perforated synapses and enlarged postsynaptic densities in Lgals4-KO mice. (A) Representative electron micrographs and synaptic density quantifications of total synapses (upper panels), shaft synapses (middle panels), and perforated synapses (bottom panels) in the *stratum radiatum* of WT and Lgals4-KO mice. The arrows indicate synapses marked by the presence of PSDs. Total and shaft synaptic densities were comparable between WT and Lgals4-KO mice (Unpaired t-test; p=0.3171 for total synapses, p=0.7532 for shaft synapses), while the density of perforated synapses was significantly increased in Lgals4-KO mice (Unpaired t-test, **p=0.0011). A total of 2143 synapses from 6 WT mice and 2540 synapses from 6 KO mice were analyzed. Data in bar graphs are mean + SEM. Dots in bar graphs represent the mean value per animal. Scale bars: 500 nm. (B) Illustrative electron micrographs highlighting the PSD area (cyan) and PSD length (red) measured and quantified in C and D, respectively. Scale bar: 200 nm. (C) Cumulative frequency distribution of PSD areas. Note that the cumulative frequency plot is shifted rightward in Lgals4-KO mice, indicating a greater proportion of PSDs with an increased size (Kolmogorov-Smirnov test; **p=0.0026). The inset shows a dot plot of each PSD area measured in the analysis for both strains (Mann-Whitney U test; ***p<0.0001). (D) Cumulative frequency distribution of PSD lengths. The cumulative frequency plot exhibits comparable PSD lengths across both experimental groups (Kolmogorov-Smirnov test; p=0.1951). The inset displays a scatter plot of each PSD length measured in the analysis for both WT and Lgals4-KO mice (Mann-Whitney U test; p=0.1045). A total of 870 synapses from 6 WT mice and 930 synapses from 6 KO mice were analyzed.

References

Acosta MP & Lepenies B (2019) Bacterial glycans and their interactions with lectins in the innate immune system. *Biochem Soc Trans* 47: 1569–1579

An G, Wei B, Xia B, McDaniel JM, Ju T, Cummings RD, Braun J & Xia L (2007) Increased susceptibility to colitis and colorectal tumors in mice lacking core 3–derived O-glycans. *J Exp Med* 204: 1417–1429

Barondes SH, Cooper DN, Gitt MA & Leffler H (1994) Galectins. Structure and function of a large family of animal lectins. *J Biol Chem* 269: 20807–20810

Benakis C, Martin-Gallausiaux C, Trezzi J-P, Melton P, Liesz A & Wilmes P (2020) The microbiome-gut-brain axis in acute and chronic brain diseases. *Curr Opin Neurobiol* 61: 1–9

Bonetto G, Belin D & Káradóttir RT (2021) Myelin: A gatekeeper of activity-dependent circuit plasticity? *Science* 374: eaba6905

Borczyk M, Śliwińska MA, Caly A, Bernas T & Radwanska K (2019) Neuronal plasticity affects correlation between the size of dendritic spine and its postsynaptic density. *Sci Rep* 9: 1693

Bosch M & Hayashi Y (2012) Structural plasticity of dendritic spines. *Curr Opin Neurobiol* 22: 383–388

Brewer CF (2002) Binding and cross-linking properties of galectins. *Biochim Biophys Acta* 1572: 255–262

Brocca ME, Mora-Rubio A, Alonso-Calviño E, Fernández-López E, Díez-Revuelta N, Martos-Puñal D, Aguilar J, Higuero AM & Abad-Rodriguez J (2022) Normal Cortical Myelination in Galectin-4-Deficient Mice. *Cells* 11: 3485

Brocca ME, Pietranera L, Beauquis J & Nicola AFD (2013) Estradiol increases dendritic length and spine density in CA1 neurons of the hippocampus of spontaneously hypertensive rats: a Golgi impregnation study. *Exp Neurol* 247: 158–64

Can A, Dao DT, Arad M, Terrillion CE, Piantadosi SC & Gould TD (2011) The Mouse Forced Swim Test. *J Vis Exp*: e3638

Can A, Dao DT, Terrillion CE, Piantadosi SC, Bhat S & Gould TD (2012) The tail suspension test. *JoVE*: e3769

Chater TE & Goda Y (2014) The role of AMPA receptors in postsynaptic mechanisms of synaptic plasticity. *Front Cell Neurosci* 8: 401

Chen P, Ban W, Wang W, You Y & Yang Z (2023) The Devastating Effects of Sleep Deprivation on Memory: Lessons from Rodent Models. *Clocks Sleep* 5: 276–294

Chu C, Murdock MH, Jing D, Won TH, Chung H, Kressel AM, Tsaava T, Addorisio ME, Putzel GG, Zhou L, *et al* (2019) The microbiota regulate neuronal function and fear extinction learning. *Nature*: 1–24

Díez-Revuelta N, Higuero AM, Velasco S, Peñas-de-la-Iglesia M, Gabius H-J & Abad-Rodriguez J (2017) Neurons define non-myelinated axon segments by the regulation of galectin-4-containing axon membrane domains. *Sci Rep* 7: 12246

Forster SC, Clare S, Beresford-Jones BS, Harcourt K, Notley G, Stares MD, Kumar N, Soderholm AT, Adoum A, Wong H, *et al* (2022) Identification of gut microbial species linked with disease variability in a widely used mouse model of colitis. *Nat Microbiol* 7: 590–599

Foster JA & Neufeld K-AM (2013) Gut–brain axis: how the microbiome influences anxiety and depression. *Trends Neurosci* 36: 305–312

Fu J, Wei B, Wen T, Johansson MEV, Liu X, Bradford E, Thomsson KA, McGee S, Mansour L, Tong M, *et al* (2011) Loss of intestinal core 1–derived O-glycans causes spontaneous colitis in mice. *J Clin Investig* 121: 1657–1666

Gipson CD & Olive MF (2017) Structural and functional plasticity of dendritic spines – root or result of behavior? *Genes, Brain Behav* 16: 101–117

Harris KM (2020) Structural LTP: from synaptogenesis to regulated synapse enlargement and clustering. *Curr Opin Neurobiol* 63: 189–197

Heijtz RD, Wang S, Anuar F, Qian Y, Björkholm B, Samuelsson A, Hibberd ML, Forssberg H & Pettersson S (2011) Normal gut microbiota modulates brain development and behavior. *Proc Natl Acad Sci USA* 108: 3047–3052

Hoban AE, Stilling RM, Ryan FJ, Shanahan F, Dinan TG, Claesson MJ, Clarke G & Cryan JF (2016) Regulation of prefrontal cortex myelination by the microbiota. *Transl Psychiatry* 6: e774–e774

Ideo H, Seko A, Ohkura T, Matta KL & Yamashita K (2002) High-affinity binding of recombinant human galectin-4 to SO3-Galbeta1,3GalNAc pyranoside. *Glycobiology* 12: 199–208

Ideo H, Seko A & Yamashita K (2005) Galectin-4 Binds to Sulfated Glycosphingolipids and Carcinoembryonic Antigen in Patches on the Cell Surface of Human Colon Adenocarcinoma Cells. *J Biol Chem* 280: 4730–4737

Ideo H, Seko A & Yamashita K (2007) Recognition mechanism of galectin-4 for cholesterol 3-sulfate. *J Biol Chem* 282: 21081–21089

Johansson MEV, Sjövall H & Hansson GC (2013) The gastrointestinal mucus system in health and disease. *Nat Rev Gastroenterol Hepatol* 10: 352–361

Jong H de, Wösten MMSM & Wennekes T (2021) Sweet impersonators: Molecular mimicry of host glycans by bacteria. *Glycobiology* 32: 11–22

Kasai K & Hirabayashi J (1996) Galectins: a family of animal lectins that decipher glycocodes. 119: 1–8

Kudelka MR, Stowell SR, Cummings RD & Neish AS (2020) Intestinal epithelial glycosylation in homeostasis and gut microbiota interactions in IBD. *Nat Rev Gastroenterol Hepatol* 17: 597–617

Kutzner TJ, Higuero AM, Süßmair M, Hingar M, Kaltner H, Lindner I, Kopitz J, Abad-Rodriguez J, Reusch D & Gabius H-J (2022) What Happens If a Human Galectin Enters the Endoplasmic Reticulum? *Methods Mol Biol* 2442: 247–288

Kutzner TJ, Higuero AM, Süßmair M, Kopitz J, Hingar M, Díez-Revuelta N, Caballero GG, Kaltner H, Lindner I, Abad-Rodriguez J, *et al* (2020) How presence of a signal peptide affects human galectins-1 and -4: Clues to explain common absence of a leader sequence among adhesion/growth-regulatory galectins. *Biochim Biophys Acta Gen Subj* 1864: 129449

Lee H-K, Takamiya K, He K, Song L & Huganir RL (2010) Specific Roles of AMPA Receptor Subunit GluR1 (GluA1) Phosphorylation Sites in Regulating Synaptic Plasticity in the CA1 Region of Hippocampus. *J Neurophysiol* 103: 479–489

Li C-S, Lo T-H, Tu T-J, Chueh D-Y, Yao C-I, Lin C-H, Chen P & Liu F-T (2023) Cytosolic galectin-4 enchains bacteria, restricts their motility, and promotes inflammasome activation in intestinal epithelial cells. *Proc Natl Acad Sci USA* 120: e2207091120

Lin S, Zhou Z, Qi Y, Chen J, Xu G, Shi Y, Yu Z, Li M & Chai K (2024) Depression promotes breast cancer progression by regulating amino acid neurotransmitter metabolism and gut microbial disturbance. *Clin Transl Oncol* 26: 1407–1418

Lisman J, Yasuda R & Raghavachari S (2012) Mechanisms of CaMKII action in long-term potentiation. *Nat Rev Neurosci* 13: 169–182

Livak KJ & Schmittgen TD (2001) Analysis of relative gene expression data using real-time quantitative PCR and the 2(-Delta Delta C(T)) Method. *Methods* 25: 402–408

Lu J, Synowiec S, Lu L, Yu Y, Bretherick T, Takada S, Yarnykh V, Caplan J, Caplan M, Claud EC, *et al* (2018) Microbiota influence the development of the brain and behaviors in C57BL/6J mice. *PLoS ONE* 13: e0201829

Mabrok HB, Ramadan AA, Hamed IM & Mohamed DA (2024) Obesity as Inducer of Cognitive Function Decline via Dysbiosis of Gut Microbiota in Rats. *Brain Sci* 14: 807

Malinow R (2003) AMPA receptor trafficking and long-term potentiation. *Philos Trans R Soc Lond, B, Biol Sci* 358: 707–714

Matsuzaki M, Honkura N, Ellis-Davies GCR & Kasai H (2004) Structural basis of long-term potentiation in single dendritic spines. *Nature* 429: 761–766

Munyeshyaka M & Fields RD (2022) Oligodendroglia are emerging players in several forms of learning and memory. *Commun Biol* 5: 1148

Needham BD, Funabashi M, Adame MD, Wang Z, Boktor JC, Haney J, Wu W-L, Rabut C, Ladinsky MS, Hwang S-J, *et al* (2022) A gut-derived metabolite alters brain activity and anxiety behaviour in mice. *Nature* 602: 647–653

Nicoll RA (2017) A Brief History of Long-Term Potentiation. *Neuron* 93: 281–290

Noguchi J, Matsuzaki M, Ellis-Davies GCR & Kasai H (2005) Spine-Neck Geometry Determines NMDA Receptor-Dependent Ca2+ Signaling in Dendrites. *Neuron* 46: 609–622

Oda Y, Herrmann J, Gitt MA, Turck CW, Burlingame AL, Barondes SH & Leffler H (1993) Soluble lactose-binding lectin from rat intestine with two different carbohydrate-binding domains in the same peptide chain. *J Biol Chem* 268: 5929–5939

Opazo P, Labrecque S, Tigaret CM, Frouin A, Wiseman PW, Koninck PD & Choquet D (2010) CaMKII triggers the diffusional trapping of surface AMPARs through phosphorylation of stargazin. *Neuron* 67: 239–252

Paiva IHR de, Silva RS da, Mendonça IP, Souza JRB de & Peixoto CA (2024) Semaglutide Attenuates Anxious and Depressive-Like Behaviors and Reverses the Cognitive Impairment in a Type 2 Diabetes Mellitus Mouse Model Via the Microbiota-Gut-Brain Axis. *J Neuroimmune Pharmacol* 19: 36

Palepu MSK, Gajula SNR, K M, Sonti R & Dandekar MP (2024) SCFAs Supplementation Rescues Anxiety- and Depression-like Phenotypes Generated by Fecal Engraftment of Treatment-Resistant Depression Rats. *ACS Chem Neurosci* 15: 1010–1025

Park J, Chávez AE, Mineur YS, Morimoto-Tomita M, Lutzu S, Kim KS, Picciotto MR, Castillo PE & Tomita S (2016) CaMKII Phosphorylation of TARPγ-8 Is a Mediator of LTP and Learning and Memory. *Neuron* 92: 75–83

Pelaseyed T & Hansson GC (2020) Membrane mucins of the intestine at a glance. *J Cell Sci* 133

Pessoa J, Belew GD, Barroso C, Egas C & Jones JG (2023) The Gut Microbiome Responds Progressively to Fat and/or Sugar-Rich Diets and Is Differentially Modified by Dietary Fat and Sugar. *Nutrients* 15: 2097

Rausch P, Rehman A, Künzel S, Häsler R, Ott SJ, Schreiber S, Rosenstiel P, Franke A & Baines JF (2011) Colonic mucosa-associated microbiota is influenced by an interaction of Crohn disease and FUT2 (Secretor) genotype. *Proc Natl Acad Sci* 108: 19030–19035

Rustiguel JK, Soares ROS, Meisburger SP, Davis KM, Malzbender KL, Ando N, Dias-Baruffi M & Nonato MC (2016) Full-length model of the human galectin-4 and insights into dynamics of inter-domain communication. *Sci Rep* 6: 1–13

Shepherd JD & Huganir RL (2007) The cell biology of synaptic plasticity: AMPA receptor trafficking. *Annu Rev Cell Dev Biol* 23: 613–643

Sorra KE & Harris KM (1998) Stability in Synapse Number and Size at 2 Hr after Long-Term Potentiation in Hippocampal Area CA1. *J Neurosci* 18: 658–671

Stancic M, Slijepcevic D, Nomden A, Vos MJ, Jonge JCD, Sikkema AH, Gabius H-J, Hoekstra D & Baron W (2012) Galectin-4, a novel neuronal regulator of myelination. *Glia* 60: 919–935

Sterio DC (1984) The unbiased estimation of number and sizes of arbitrary particles using the disector. *J Microsc* 134: 127–136

Stowell SR, Arthur CM, Dias-Baruffi M, Rodrigues LC, Gourdine J-P, Heimburg-Molinaro J, Ju T, Molinaro RJ, Rivera-Marrero C, Xia B, *et al* (2010) Innate immune lectins kill bacteria expressing blood group antigen. *Nat Med* 16: 295–301

Stowell SR, Arthur CM, McBride R, Berger O, Razi N, Heimburg-Molinaro J, Rodrigues LC, Gourdine J-P, Noll AJ, Gunten S von, *et al* (2014) Microbial glycan microarrays define key features of host-microbial interactions. *Nat Chem Biol* 10: 470–476

Sugio S, Kato D & Wake H (2023) Myelinated axon as a plastic cable regulating brain functions. *Neurosci Res* 187: 45–51

Sumi T & Harada K (2020) Mechanism underlying hippocampal long-term potentiation and depression based on competition between endocytosis and exocytosis of AMPA receptors. *Sci Rep* 10: 14711

Sun Y, Smirnov M, Kamasawa N & Yasuda R (2021) Rapid Ultrastructural Changes in the PSD and Surrounding Membrane after Induction of Structural LTP in Single Dendritic Spines. *J Neurosci* 41: 7003–7014

Tobisawa Y, Imai Y, Fukuda M & Kawashima H (2010) Sulfation of Colonic Mucins by N-Acetylglucosamine 6-O-Sulfotransferase-2 and Its Protective Function in Experimental Colitis in Mice*. *J Biol Chem* 285: 6750–6760

Tran SM-S & Mohajeri MH (2021) The Role of Gut Bacterial Metabolites in Brain Development, Aging and Disease. *Nutrients* 13: 732

Velasco S, Díez-Revuelta N, Hernández-Iglesias T, Kaltner H, André S, Gabius H-J & Abad-Rodriguez J (2013) Neuronal Galectin-4 is required for axon growth and for the organization of axonal membrane L1 delivery and clustering. *Journal of Neurochemistry* 125: 49–62

Vuong HE, Yano JM, Fung TC & Hsiao EY (2016) The Microbiome and Host Behavior. *Annu Rev Neurosci* 40: 1–29

Wei Q, Eviatar-Ribak T, Miskimins WK & Miskimins R (2007) Galectin-4 is involved in p27-mediated activation of the myelin basic protein promoter. *Journal of Neurochemistry* 101: 1214–1223

Yamasaki M, Fukaya M, Yamazaki M, Azechi H, Natsume R, Abe M, Sakimura K & Watanabe M (2016) TARP γ-2 and γ-8 Differentially Control AMPAR Density Across Schaffer Collateral/Commissural Synapses in the Hippocampal CA1 Area. *J Neurosci* 36: 4296–4312

Yan W, Zhuang Z, Gao Y, Wang Y & He D (2024) A Mendelian randomization investigation of the causal association between the gut microbiota and sleep disorders. *Front Microbiol* 15: 1372827

Yin J, John A & Cadar D (2024) Bidirectional Associations of Depressive Symptoms and Cognitive Function Over Time. *JAMA Netw Open* 7: e2416305

Zhang N, Gao X, Li D, Xu L, Zhou G, Xu M, Peng L, Sun G, Pan F, Li Y, *et al* (2024) Sleep deprivation-induced anxiety-like behaviors are associated with alterations in the gut microbiota and metabolites. *Microbiol Spectr* 12: e01437-23

Zhang Y, Wang L, Ocansey DKW, Wang B, Wang L & Xu Z (2021) Mucin-Type O-Glycans: Barrier, Microbiota, and Immune Anchors in Inflammatory Bowel Disease. *J Inflamm Res* 14: 5939–5953

Figure 1

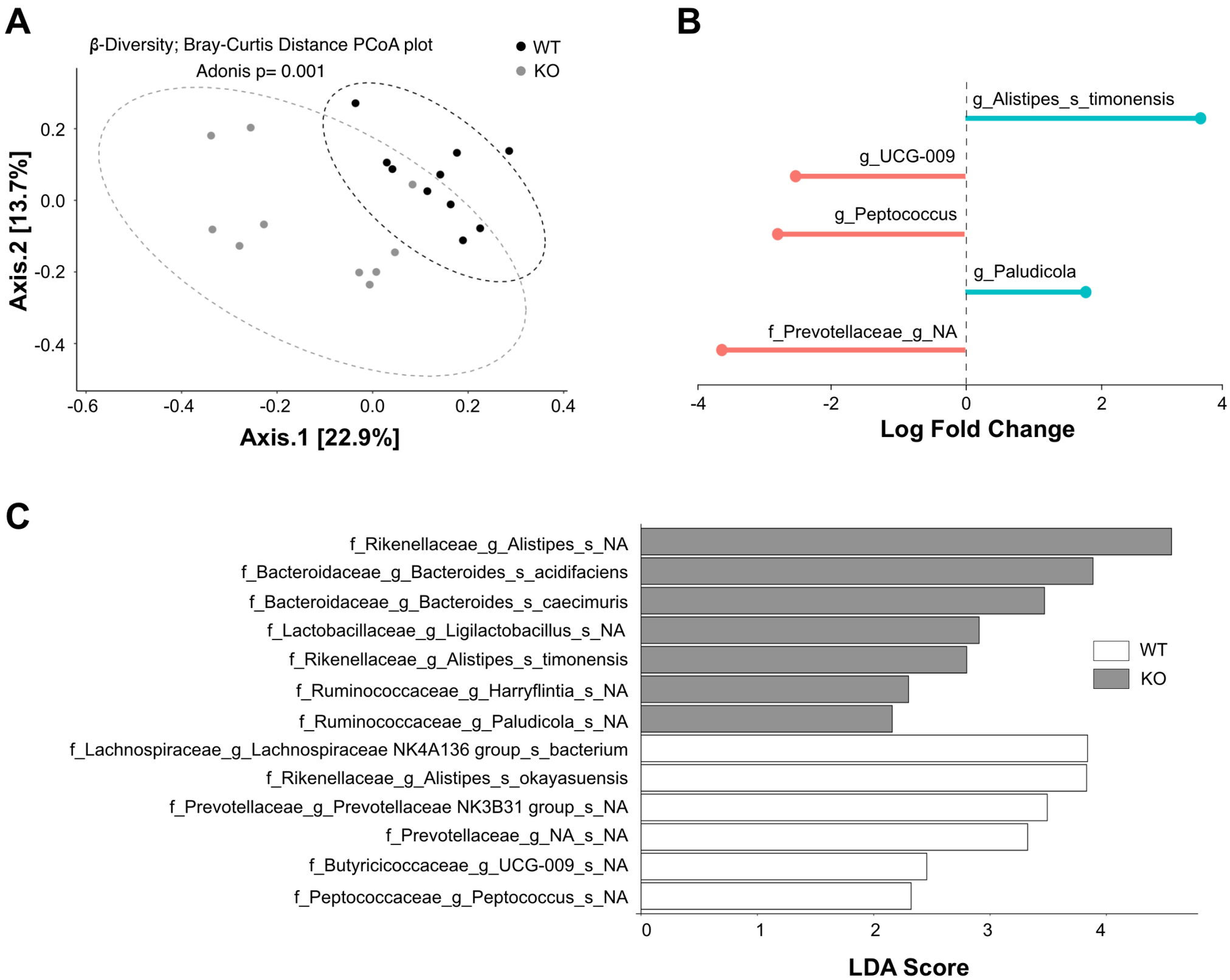
A
β-Diversity; Bray-Curtis Distance PCoA plot
Adonis p= 0.001
WT
KO
Axis.2 [13.7%]
Axis.1 [22.9%]
0.2
0.0
-0.2
-0.4
-0.6
-0.4
-0.2
0.0
0.2
0.4
B
g_Alistipes_s_timonensis
g_UCG-009
g_Peptococcus
g_Paludicola
f_Prevotellaceae_g_NA
-4
-2
0
2
4
Log Fold Change
C
f_Rikenellaceae_g_Alistipes_s_NA
f_Bacteroidaceae_g_Bacteroides_s_acidifaciens
f_Bacteroidaceae_g_Bacteroides_s_caecimuris
f_Lactobacillaceae_g_Ligilactobacillus_s_NA
f_Rikenellaceae_g_Alistipes_s_timonensis
f_Ruminococcaceae_g_Harryflintia_s_NA
f_Ruminococcaceae_g_Paludicola_s_NA
f_Lachnospiraceae_g_Lachnospiraceae NK4A136 group_s_bacterium
f_Rikenellaceae_g_Alistipes_s_okayasuensis
f_Prevotellaceae_g_Prevotellaceae NK3B31 group_s_NA
f_Prevotellaceae_g_NA_s_NA
f_Butyricicoccaceae_g_UCG-009_s_NA
f_Peptococcaceae_g_Peptococcus_s_NA
WT
KO
0
1
2
3
4
LDA Score

Figure 2

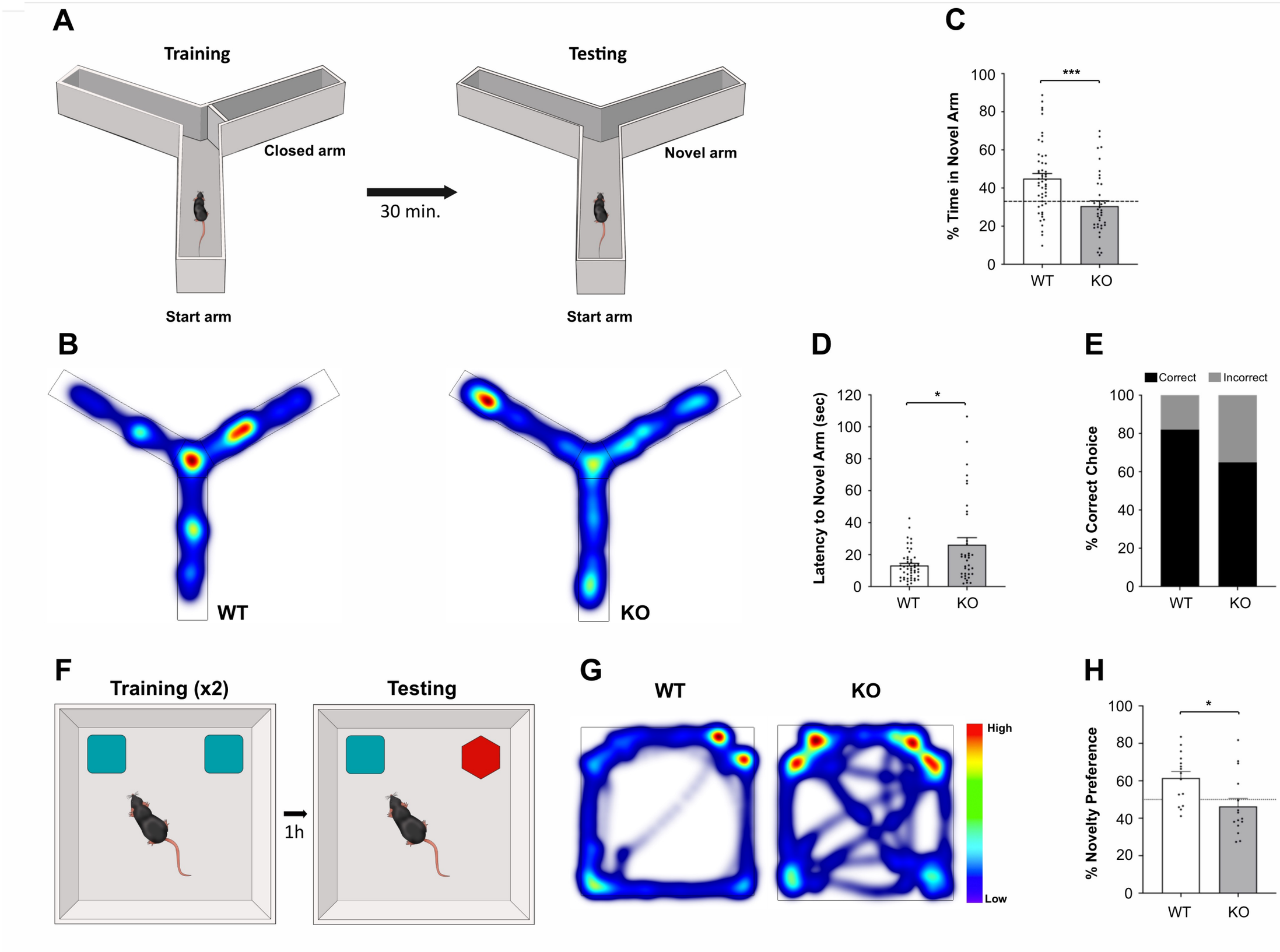
A
Training
Closed arm
Start arm
30 min.
Testing
Novel arm
Start arm
B
WT
KO
C
% Time in Novel Arm
***
WT
KO
D
Latency to Novel Arm (sec)
*
WT
KO
E
Correct
Incorrect
% Correct Choice
WT
KO
F
Training (x2)
1h
Testing
G
WT
KO
High
Low
H
% Novelty Preference
*
WT
KO

Figure 3

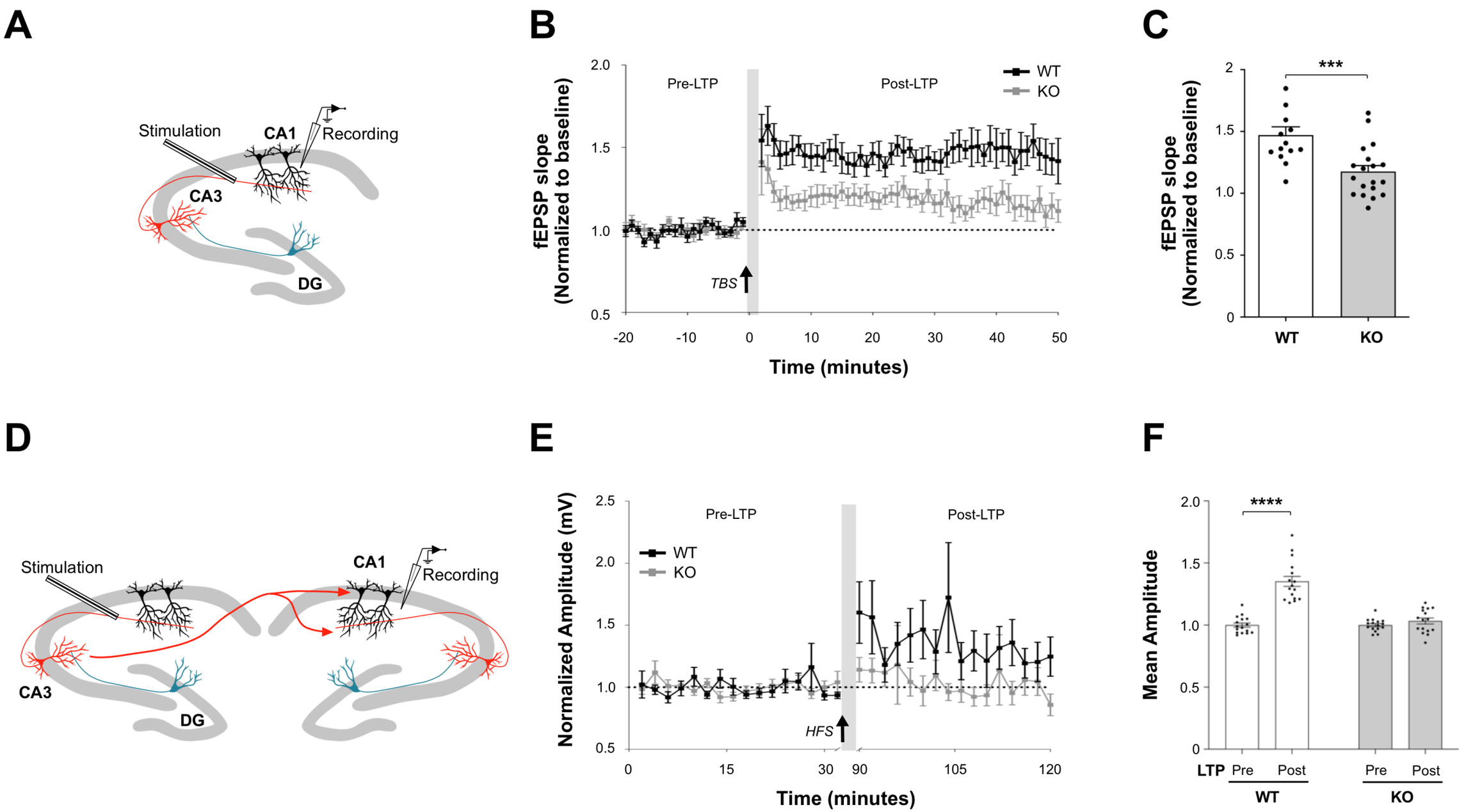
A
Stimulation
CA1
Recording
CA3
DG
B
fEPSP slope
(Normalized to baseline)
Pre-LTP
Post-LTP
WT
KO
TBS
Time (minutes)
C
fEPSP slope
(Normalized to baseline)
***
WT
KO
D
Stimulation
CA1
Recording
CA3
DG
E
Normalized Amplitude (mV)
Pre-LTP
Post-LTP
WT
KO
HFS
Time (minutes)
F
Mean Amplitude
****
LTP
Pre
Post
Pre
Post
WT
KO

Figure 4

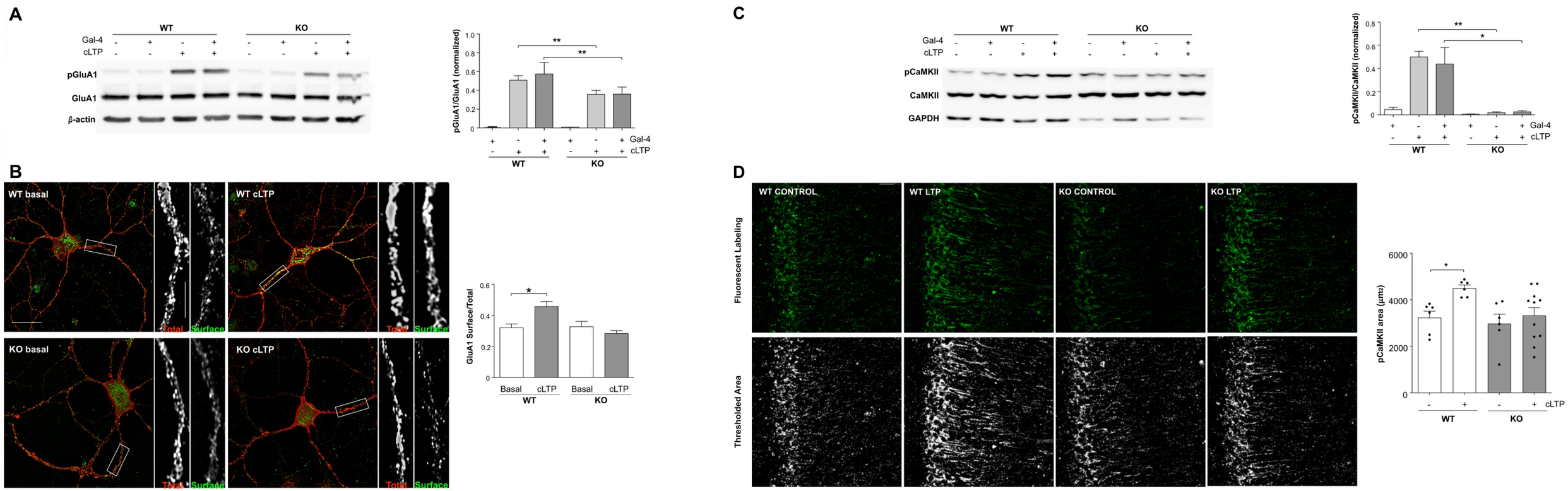
A
WT
KO
Gal-4
cLTP
pGluA1
GluA1
β-actin
pGluA1/GluA1 (normalized)
Gal-4
cLTP
B
WT basal
WT cLTP
KO basal
KO cLTP
Total
Surface
GluA1 Surface/Total
Basal
cLTP
C
pCaMKII
CaMKII
GAPDH
pCaMKII/CaMKII (normalized)
D
WT CONTROL
WT LTP
KO CONTROL
KO LTP
Fluorescent Labeling
Thresholded Area
pCaMKII area (μm2)

Figure 5

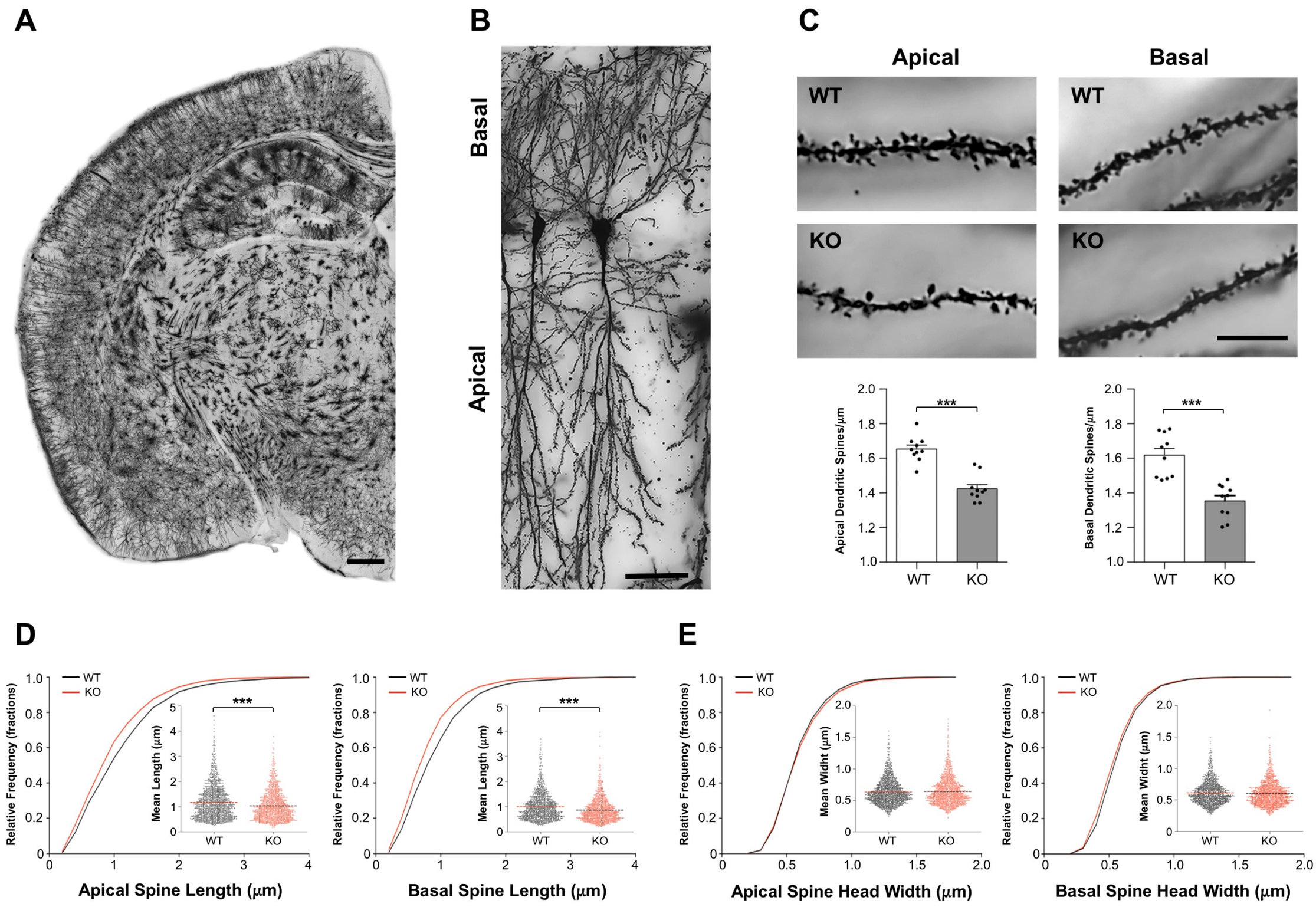
A
B
Basal
Apical
C
Apical
Basal
WT
KO
Apical Dendritic Spines/μm
Basal Dendritic Spines/μm
***
D
E
Relative Frequency (fractions)
Mean Length (μm)
Mean Widht (μm)
Apical Spine Length (μm)
Basal Spine Length (μm)
Apical Spine Head Width (μm)
Basal Spine Head Width (μm)

Figure 6

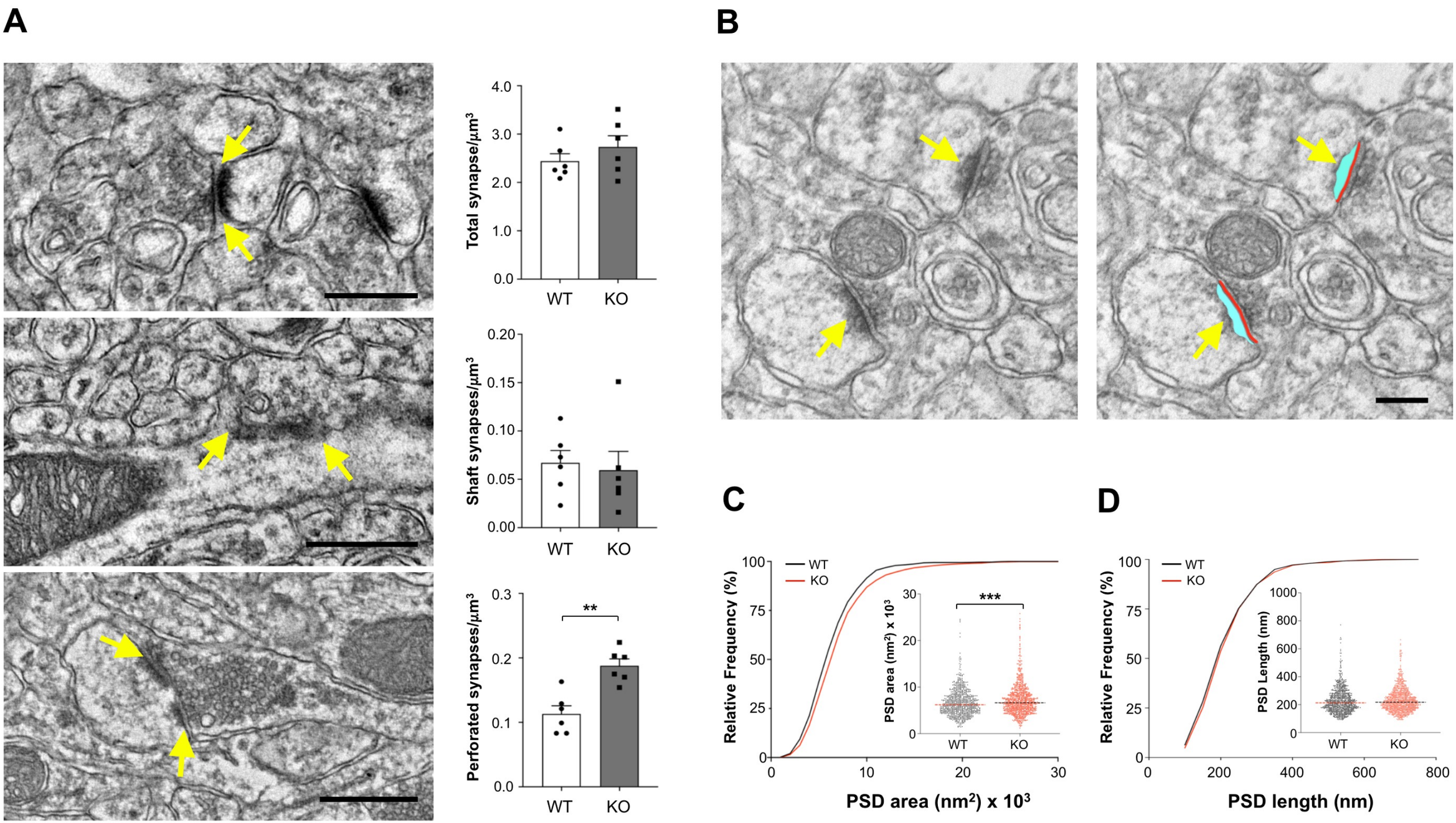
A
B
C
D
Total synapse/μm³
Shaft synapses/μm³
Perforated synapses/μm³
WT
KO
**
Relative Frequency (%)
PSD area (nm²) x 10³
PSD Length (nm)
PSD length (nm)
***